



저작자표시-비영리-변경금지 2.0 대한민국

이용자는 아래의 조건을 따르는 경우에 한하여 자유롭게

- 이 저작물을 복제, 배포, 전송, 전시, 공연 및 방송할 수 있습니다.

다음과 같은 조건을 따라야 합니다:



저작자표시. 귀하는 원저작자를 표시하여야 합니다.



비영리. 귀하는 이 저작물을 영리 목적으로 이용할 수 없습니다.



변경금지. 귀하는 이 저작물을 개작, 변형 또는 가공할 수 없습니다.

- 귀하는, 이 저작물의 재이용이나 배포의 경우, 이 저작물에 적용된 이용허락조건을 명확하게 나타내어야 합니다.
- 저작권자로부터 별도의 허가를 받으면 이러한 조건들은 적용되지 않습니다.

저작권법에 따른 이용자의 권리는 위의 내용에 의하여 영향을 받지 않습니다.

이것은 [이용허락규약\(Legal Code\)](#)을 이해하기 쉽게 요약한 것입니다.

[Disclaimer](#)

Thesis of Master Degree

**A Study on Electrical Transport Properties of
ZnTe Buffer Layer Effect on Tellurium Doped
GaSb:Te Epitaxial Layer**

Supervisor: Professor Hong Chan Lee

2009-02

Graduate School of Korea Maritime University

Department of Mechatronics Engineering

Aung Khaing Nyi

Abstract

Among the III-V binary semiconductors, Gallium Antimonide (GaSb) has attracted considerable attention. Many of its interesting properties are directly associated with its very low effective electron mass and high mobility. Consequently, it is an important candidate in high speed applications in transistors and other devices.

Undoped GaSb is always p-type conductivity due to the native defect such as Sb vacancy. Therefore, to achieve n-type thin film with higher carrier mobility, high quality film growth is absolutely required.

This thesis presents the electrical transport properties for one typical set of Te-doped GaSb layers; the one is normally grown on a GaAs substrate by molecular-beam epitaxy (Type I), and the other includes a ZnTe buffer between the GaSb:Te layer and the GaAs substrate (Type II) with the structural properties and investigated the effect of ZnTe buffer on the Te-doped GaSb epitaxial layers based on the two layer Hall effect model. The five major scattering mechanisms (ionized impurity, dislocation, piezoelectric, deformation potential and polar phonon) effects were considered.

By using this method, two types of GaSb:Te layers show extremely different electrical and structural properties; i) Type I has an electron mobility of $250 \text{ cm}^2/\text{V}\cdot\text{s}$, while Type II has 2.5 times larger value, ($630 \text{ cm}^2/\text{V}\cdot\text{s}$); ii) Type I has a X-ray linewidth of 970 arcsec, while Type II has 2 times smaller value (520 arcsec). The increase of electron mobility in Type II is ascribed to the suppression of defect scatterings by point defects and dislocations, which is consistent to the decrease of X-ray linewidth in Type II. The electron transport mechanisms of the two types of GaSb:Te layers can be explained by ionized-impurity scattering and dislocation scattering. Consequently, it is suggested that the ZnTe buffer layers effectively

enhance the structural quality and carrier mobility in Te-doped n-type GaSb epitaxial layers, which will improve the fabrication of optoelectronic devices.



Acknowledgements

First and foremost, I wish to express my deepest gratitude to my dissertation advisor, Professor Hong Chan Lee of Mechatronics Department for all his valuable guidance, assistance and support throughout my graduate studies at the Korea Maritime University. It was Professor Lee who introduced me to this field and helped me to understand this technology.

I would like to thank my Professor Ji Ho Chang. He has influenced and inspired this research in many ways, both direct and indirect. In discussing my work, he has always had insightful comments, helpful ideas and an unerring ability to identify the key elements in complex problems.

I am grateful to Professor Dong Cheol Oh for several helpful and competent discussions as well as for his support and guidance during my work.

It is my pleasure to express my great appreciation the members of my thesis defense committee: Professor Hong Seung Kim, Professor Hong Chang Lee and Professor Sang Tae Lee. I have profited from their advice, enthusiasm and attitude toward life. Professor Kim has always been encouraging, cheerful, and approachable and a source of thoughtful counsel also my grateful go to Professor Sang Tae Lee who chaired my thesis defense committee, I thank him for giving me the tools to do dynamics.

I owe a special debt to Professor Kyawt Khin and Professor Zaw Min Aung of Yangon Institute of Technology, who introduced me to Professor Hong Chang Lee for study in Korea.

My special thanks go to Si Young Kim and Woong Lee, who were always there to help me in learning about the Molecular Beam Epitaxy (MBE). I wish to

thank the members of Nano Material and Device Lab for their suggestions and support on this research. Their comments on this research are greatly appreciated.

My special thanks to Duy Ahn Nguyen, Ngo Thanh Hoan, both of whom are Vietnamese students at this university, Kyaw Soe Lwin, Ye Min Hein and Aye Thida Aung for numerous assistance I received during this project.

Acknowledgements must also go to Lee Kyong Huh, Jung Hwan Moon and Ha Yong Chang from my department office for helping me in getting used to a foreign country and for their continuous support and encouragement.

My great appreciation is also extended to Myanmar students from Korea Maritime University has been a great deal more than equations and computers and for this I have to thank the many people I have come to know and call friends.

A debt of gratitude goes to Phyu Phyu Aung, Information Studies Division, Wee Kim Wee School of Communication and Information, NTU, Singapore for supporting the valuable references for my research study during these years.

The one who love and support have meant more than I know how to say. She adds dimension and perspective to my life and it is with much anticipation and excitement for our future.

Finally, my heartfelt gratitude also goes to my parents and family, who have always been a source of constant support and encouragement in my pursuit for achieving excellence in all my career goals that I dedicate this thesis to them.

Table of Contents

Abstract	i
Acknowledgment	iii
Table of Contents	v
List of Figures	viii
List of Tables	xii
Chapter 1 Introduction	1
1.1 Historical background of Gallium Antimonide.....	1
1.2 Purpose and composition of the thesis.....	4
Chapter 2 Properties of Gallium Antimonide	7
2.1 Structural properties.....	7
2.1.1 Lattice parameter.....	7
2.1.2 Density.....	7
2.1.3 Crystal structure.....	7
2.2 Thermal properties.....	8
2.2.1 Heat capacity and Debye temperature.....	8
2.2.2 Elastic moduli and phonon dispersion.....	10
2.2.3 Thermal expansion.....	13
2.2.4 Thermal conductivity.....	14
2.3 Electronic and transport properties.....	17

2.3.1	Band structure	17
2.3.2	Effective masses of electrons and holes.....	22
2.3.3	Electron transport.....	24
2.3.4	Hole transport.....	29
Chapter 3 Growth of GaSb:Te epilayers on GaAs (001) substrate		36
3.1	Introduction	36
3.1.1	Zinc Telluride (ZnTe) buffer layer.....	36
3.1.2	Elemental Tellurium (Te) dopant source	39
3.2	Molecular Beam Epitaxial growth techniques	40
3.2.1	Overview of the MBE growth chamber.....	40
3.2.2	Reflection High Energy Electron Diffraction (RHEED)	42
3.2.3	MBE growth procedures	44
3.2.4	Fabrication of the high quality n-type GaSb:Te epitaxial layers ...	45
3.3	Hall Effect measurement	46
3.3.1	Experimental setup of Hall measurement	46
3.3.2	Hall Effects	47
3.3.3	Van der Pauw method	49
3.4	High-resolution X-ray Diffraction (HRXRD) measurement.....	50
3.4.1	Experimental setup of HRXRD	50
3.4.2	ω scan (rocking curve) and ω - 2θ scan	51
Chapter 4 Electrical transport properties of GaSb:Te epitaxial layers		55
4.1	Introduction	55

4.2	Structural properties of GaSb:Te epitaxial layers	57
4.3	Electrical properties of GaSb:Te epitaxial layers	59
4.4	Correction by two-layer Hall Effect model	63
4.5	Fitting of temperature dependent carrier concentration curves	65
4.6	Calculation of mobility curves by the Boltzman transport equations	68
4.6.1	Ionized impurity scattering	68
4.6.2	Dislocation Scattering	70
4.6.3	Acoustic phonon: deformation potential	70
4.6.4	Acoustic phonons: piezoelectric potential	71
4.6.5	Optical phonons: polar	72
4.6.6	Matthiessen's rule	72
Chapter 5	Conclusion	75
References	75



List of Figures

Fig. 1.1	Band gap as a function of lattice constant for III–V compounds and their ternary and quaternary alloys.	2
Fig. 2.1	Comparison of heat capacity of GaSb calculated from $g(\nu)$ with the experimental data.....	9
Fig. 2.2	Comparison of the Debye temperature for GaSb calculated from $g(\nu)$ with experiment data.....	9
Fig. 2.3	Temperature dependence of second–order elastic moduli.	11
Fig. 2.4	Phonon dispersion relation for GaSb.....	11
Fig. 2.5	First-order Stokes Raman spectra for GaSb taken with the 5309Å laser line at different pressure.....	12
Fig. 2.6	Dependence of the TO and LO phonon frequencies of GaSb on linear lattice compression and pressure.....	12
Fig. 2.7	Temperature dependence of linear thermal expansion coefficient of GaSb from 4.2 to 340 K.	13
Fig. 2.8	Temperature dependence of linear thermal expansion coefficient of GaSb above room temperature.....	14
Fig. 2.9	Temperature dependence of Grüneisen parameter for GaSb.	14
Fig. 2.10	Thermal conductivity of GaSb for n- and p-type samples..	15
Fig. 2.11	High temperature thermal conductivity of GaSb.....	16
Fig. 2.12	Band structure of GaSb.	17

Fig. 2.13	Energies of electroreflectance peaks as a function of temperature	19
Fig. 2.14	Temperature dependence of electron mobility in Γ and L band for GaSb.....	24
Fig. 2.15	(a) Transverse and (b) longitudinal magnetoresistance oscillations at various temperatures for Te-doped n-GaSb samples after Li diffusion.....	28
Fig. 2.16	Heavy hole density of states effective mass as a function of reciprocal temperature.....	29
Fig. 2.17	Hole mobility as a function of temperature.....	30
Fig. 2.18	Hole mobility as a function of temperature for undoped p-GaSb grown from stoichiometric melt, undoped p-GaSb grown from Ga-rich melt, undoped p-GaSb grown from Sb-rich melt, and Te-compensated p-GaSb to various degrees.....	31
Fig. 2.19	Temperature variation of theoretically calculated partial mobilities and effective mobility for undoped p-GaSb.....	32
Fig. 2.20	Temperature variation of theoretically calculated partial mobilities and effective mobility for a typical heavily Te- compensated p-GaSb.....	32
Fig. 2.21	Plot of intrinsic carrier concentration as a function of temperature for undoped p-GaSb.....	33
Fig. 2.22	Mobility as a function of temperature for undoped p-GaSb above room temperature.....	34

Fig. 3.1	Experimental values of ZnTe coefficient of linear thermal expansion.....	38
Fig. 3.2	Schematic layout of a typical MBE growth chamber.....	42
Fig. 3.3	Schematic illustration of simple epitaxial growth mechanism.....	42
Fig. 3.4	Schematic illustration of typical RHEED geometry.	43
Fig. 3.5	Schematic illustration of Hall Effects measurement equipment.	47
Fig. 3.6	The sample geometry for performing Hall measurement.....	48
Fig. 3.7	Schematic diagram of Van der Pauw method.	49
Fig. 3.8	Schematic illustration of HRXRD geometry.....	51
Fig. 3.9	Diffraction of a plane corresponding to Bragg law.....	52
Fig. 3.10	Reciprocal space map showing accessible range for Bragg reflection measurements.....	53
Fig. 4.1	Williamson-Hall plot for symmetric and asymmetric reflection for using dislocation density of GaSb:Te epitaxial layers.....	58
Fig. 4.2	Temperature dependent resistivity measurement of GaSb:Te epitaxial layers.....	60
Fig. 4.3	Temperature dependent mobility measurement of GaSb:Te epitaxial layers.....	61
Fig. 4.4	Temperature dependent carrier concentration measurement of GaSb:Te epitaxial layers.....	62

Fig. 4.5 Temperature dependent measured and corrected (a) Hall concentration and (b) Hall mobility curves for the GaSb:Te epitaxial layers..... 65

Fig. 4.6 The measured and fitting carrier concentration curves for the (a) GaSb:Te/GaAs (Type I) and (b) GaSb:Te/ZnTe/GaAs (Type II) 67

Fig. 4.7 Calculated (theoretical) and measured mobilities as a function of temperature for (a) sample A- GaSb:Te/GaAs (Type I) and (b) sample B- GaSb:Te/ZnTe/GaAs (Type II)..... 74



List of Tables

Table 2.1 Energies of symmetry points of band structure relative to the top of valence band.	18
Table 2.2 Effective masses of electrons and holes.....	23
Table 2.3 The important material properties of GaSb.	35
Table 3.1 Typical properties of GaSb, ZnTe and GaAs which used in this study.....	38
Table 3.2 Thermal etching condition of GaAs substrate.	45
Table 3.3 The effect of substrate and epilayer parameters upon the rocking curve.....	54
Table 4.1 A summary of the various methods of evaluating transport properties of semiconductors.	56
Table 4.2 HRXRD measurements result of GaSb:Te epitaxial layers.....	57
Table 4.3 Temperature dependent Hall Effect measurements of GaSb:Te epitaxial layers	63

Chapter 1 Introduction

1.1 Historical background of Gallium Antimonide

Historically, the research and development of various III–V compound semiconductors is associated with the wavelength of the optical fiber loss minima.^[1] The shift in the fiber loss minima towards higher wavelengths from 0.8 μm over the past 2 decades has shifted the material of interest from time to time.^[1] Even though the present day optical communication systems are tuned to 1.55 μm , the next generation systems may have to be operated well above this wavelength. This is because recent developments in the optical fiber research have shown potentiality for certain classes of nonsilica fibers for optical communication applications whose loss minima fall in the 2–4 μm range.^[2] For example, the heavy metal fluoride glasses are speculated to have minimum attenuation at 2.55 μm with a loss, one to two orders of magnitude lower than the present day silica fibers. This is also important since, at longer wavelengths, loss due to Rayleigh scattering is significantly reduced. Consequently, there has been an up thrust in research activities in new material systems for sources and detectors operating in the 2–4 μm regime. Among compound III–V semiconductors, gallium antimonide (GaSb) is particularly interesting as a substrate material because its lattice parameter matches solid solutions of various ternary and quaternary III–V compounds whose band gaps cover a wide spectral range from ~ 0.3 to 1.58 eV,^[3] i.e., 0.8–4.3 μm , as depicted in Fig. 1.1. Also, detection of longer wavelengths, 8–14 μm , is possible with intersubband absorption in antimonide based superlattices.^[4] These have stimulated a lot of interest in GaSb for basic research as well as device fabrication.

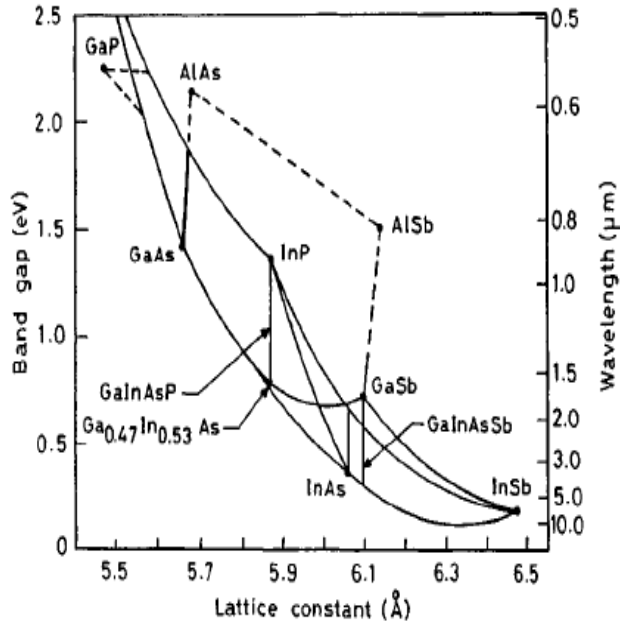


Fig. 1.1 Band gap as a function of lattice constant for III–V compounds and their ternary and quaternary alloys^[5].

From device point of view, GaSb-based structures have shown potentiality for applications in laser diodes with low threshold voltage,^[6,7] photodetectors with high quantum efficiency,^[8] high frequency devices,^[9,10] superlattices with tailored optical and transport characteristics,^[11] booster cells in tandem solar cell arrangements for improved efficiency of photovoltaic cells and high efficiency thermophotovoltaic (TPV) cells.^[12] Interestingly, the spin-orbit splitting of the valence band is almost equal to the energy band gap in GaSb leading to high hole ionization coefficients. This results in significant improvement in the signal-to-noise ratio at $\lambda > 1.3\mu\text{m}$ in GaAlSb avalanche photodetectors grown on GaSb.^[8] GaSb is also predicted to have a lattice limited electron mobility greater than GaAs making it of potential interest in the fabrication of microwave devices. InGaSb has been proposed as an ideal material for transferred-electron devices by Hilsum and Rees^[10] with a low threshold yield and a large velocity peak-to-valley ratio, using a Monte Carlo simulation based on the three-level model.

GaSb-based devices are promising candidates for a variety of military and civil applications in the 2–5 and 8–14 μm regimes:^[13] to mention a few, infrared (IR) imaging sensors for missile and surveillance systems (focal plane arrays), fire detection and monitoring environmental pollution. The absorption wavelengths of several industrial gases and water vapour lie in the near IR range for which GaSb based alloys are suitable. Gas purity monitoring and trace moisture detection in corrosive gases like HCl in semiconductor processing, detecting microleaks of toxic gases such as PH_3 , *in situ* monitoring of plasma etching, detecting hazardous gases like HF and H_2S in chemical plants, monitoring green house gas fluxes, measurements of flame species in microgravity combustion and humidity determination are a few areas where GaSb based alloys might find potential applications.^[13] Sb-based alloys can also find several biological and medical applications in the near IR regime. IR detectors in the 8–14 μm regime based on GaAlSb/AlSb and InAs/InGaSb superlattices and InAsSb are believed to be potential competitors for the present day HgCdTe detectors.^[4]

GaSb has also proved to be a model material for several basic studies.^[14] Because of the band structural properties, GaSb has proved to be an ideal material for studying the Auger recombination processes.^[15] Due to low vapour pressures and low melting points, GaSb and InGaSb serve as appropriate model materials to study the effects of convection and diffusion on the solutal distribution under terrestrial and microgravity conditions.^[16] Sulfur doped GaSb is the only III–V binary compound which reveals high concentration of donor related deep traps (commonly known as *DX* centers) at atmospheric pressure.^[14] Hence it is the most suitable material for studying the behavior of such metastable centers without the complication of high pressure or alloy broadening effects, encountered in other III–V binary and ternary alloys. Because of high concentration of native acceptors present in the as-grown unintentionally doped GaSb, it is an interesting system to study impurity compensation effects^[14]

Technological and material aspects of GaSb have sparingly been studied until now, compared to other III–V compounds, compounds, such as GaAs, InSb, InP, GaP, etc. Undoped GaSb is always *p*-type in nature irrespective of the growth technique and conditions. Work over the last 3 decades has been devoted mainly for understanding the nature and the origin of the residual acceptors which are the limiting factors for both fundamental studies and device applications. The residual acceptors with concentration of $\sim 10^{17} \text{cm}^{-3}$ have been found to be related to gallium vacancies (V_{Ga}) and gallium in antimony site (GaSb) with doubly ionizable nature.^[17] Attempts have been made to reduce their content by growing the crystals from nonstoichiometric melts.^[18] Recent studies on epitaxial layers of GaSb grown by liquid phase epitaxy^[19] and molecular beam epitaxy (MBE) with excess antimony^[20] have shown the possibility of reducing substantially the level of natural acceptors and increasing the hole mobility. This stimulated the renewed interest in growth of GaSb crystals with reduced residual acceptors.

At present, GaSb technology is in its infancy and significant progress has to be made both in materials and processing aspects before it can be employed for device applications. Current research and developments are focused on areas of high quality materials growth, better understanding of electronic and photonic properties and fabrication of suitable device structures. In this article, an overview of the basic physics of the material, preparation and processing technologies, and developments in practical device structures and their properties is presented. Certain avenues where future efforts should be concentrated in order to exploit this III–V compound for optoelectronic devices are suggested.

1.2 Purpose and composition of the thesis

In the past, native defect, complex defects, and unintentional contaminations in semiconductors have received much attention from the research community. Intentional dopants related issues received, surprisingly, much less attention.

However, the requirements for the concentration versus mobility of intentional impurities are becoming increasingly stringent in modern semiconductor technology. For example, very small semiconductor structures require doping concentrations exceeding 10^{19}cm^{-3} .

Undoped Gallium Antimonide (GaSb) is always p-type with a residual carrier density of the order of $\sim 10^{17}\text{cm}^{-3}$ due to native acceptor like defect gallium vacancies (V_{Ga}) and gallium in antimony site (Ga_{Sb}) with doubly ionized nature and the Fermi level is pinned in the GaSb valence band. Therefore, to achieve n-type thin film with high carrier mobility, high quality film growth is absolutely required.

In the recent work^[21], three-step ZnTe buffer layer improved the crystallinity of the GaSb layer with the efficient accommodation of the large lattice misfit, providing smooth surface for the GaSb layer, the reduction of residual strain and the diminishing of the structural deformation due to incomplete relaxation of strain. We grown GaSb layer with Te doping with limitation of carrier concentration and mobility by complex defect formation and GaSb:Te epitaxial layer grown on ZnTe buffer will show higher mobility.

In this study, we report on the effect of ZnTe buffers on the electrical properties of Te-doped GaSb layers grown by molecular-beam epitaxy (MBE). In order for systematic work, we discuss the electrical properties of GaSb:Te layers in conjunction with their structural properties. Finally, we investigate the scattering mechanisms that the dominate the electron transport of GaSb:Te layers using the two-layer hall effect model and analysis based on the five major scattering mechanisms, namely; polar-phonon, deformation potential, dislocation and ionized-impurity scattering.

The free-carrier distribution in semiconductors depends on the distribution of ionized impurities. The free-carrier distribution is instrumental of many properties

of semiconductors, including recombination and transport properties. In this research, we report on the effect of ZnTe buffers on the electrical properties of Te-doped GaSb layers grown by molecular-beam epitaxy (MBE). In order for systematic work, we discuss the electrical properties of GaSb:Te layers in conjunction with their structural properties. Finally, we investigate the scattering mechanisms that dominate the electron transport of GaSb:Te layers.

This thesis consists of five chapters. After this introductory Chapter 1, Chapter 2 describes the properties of Gallium Antimonide including; (1) Structural properties of Gallium Antimonide, (2) Thermal properties of Gallium Antimonide, (3) Defect and impurities of GaSb and (4) Electrical properties of GaSb.

In Chapter (3), the growth of GaSb:Te on GaAs(001) with properties and aim using ZnTe buffer layer, elemental Te source for n-type doping to GaSb epitaxial layer, and growth process of GaSb:Te layer with MBE growth technique. The Hall Effect and High resolution X-ray Diffraction method are described for the electrical properties and structural properties of the samples.

In Chapter (4), Hall measurement of GaSb:Te epitaxial layers are presented and HRXRD measurement is described with (004),(111),(115) measurements and Williamson-Hall plot showed the dislocation density of the GaSb:Te epitaxial layers. Electrical properties of GaSb:Te is explained with the Carrier concentration dependent carrier mobility with compensation ratio, using the two-layer model for the fitting of temperature dependent carrier concentration curves and the dominant scattering mechanism for the GaSb:Te layers with 5 major scattering mechanisms; (a) ionized impurity scattering, (b) dislocation scattering, (c) polar phonon scattering, (d) piezoelectric potential scattering and deformation potential scattering.

In Chapter 5, based on the results obtained from this study will present with electrical transport properties of these GaSb:Te epilayers.

Chapter 2 Properties of Gallium Antimonide

2.1 Structural properties

2.1.1 Lattice parameter

From the powder x-ray data, the lattice parameter at 25.15° C was found to be 6.09593Å.^[22] The temperature dependence of the lattice parameter up to 680° C is given by

$$a = a_0 + a_1T + a_2T^2 + a_3T^3 + a_4T^4, \quad (2.1)$$

where T is in °C. The values of the constants a_0 , a_1 , a_2 , a_3 and a_4 are 6.0959Å, 3.4963×10^{-5} Å °C⁻¹, 3.3456×10^{-8} Å °C⁻², -4.6309×10^{-11} Å °C⁻³ and 2.6369×10^{-14} °C⁻⁴, respectively.



2.1.2 Density

The density of GaSb at 300K is measured to be 5.6137 g cm⁻³.^[22] There is very little variation of density with temperature. At 900 K, it is found to be 5.60 g cm⁻³.^[23]

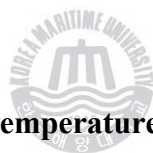
2.1.3 Crystal structure

GaSb crystallizes in zinc-blende structure, which belongs to the space group $F\bar{4}3m$ in the Hermann–Mauguin notation, or in the Schoenflies notation.^[24] The zincblende structure is identical to that of the diamond lattice except that each Ga atom has four tetrahedrally arranged Sb neighbors and vice versa. However unlike the diamond structure, the zinc-blende structure does not possess a centre of inversion, and opposite directions in the crystal are not necessarily equivalent. This leads to interesting arrangements of the atoms in the (110), (100) and (111) planes. The (100) surfaces are stepped and contain both Ga and Sb atoms. The nature of

chemical bonds in III–V compounds are of mixed covalent-ionic type. The ionicity of GaSb is 0.33. The presence of a slight ionic component in the bonds and the fact that there are have equal numbers of Ga and Sb atoms on the (110) planes results in the (110) cleavage of the compound. The zinc-blende lattice structure and partial ionic bonding impart to the crystal a polarity along the $\langle 111 \rangle$ axis. The (111) planes can be prepared with either Ga or Sb atoms on the surface. The (111) plane composed of Ga atoms is designated as (111)*A*. The $\overline{(1,1,1)}$ plane is composed of Sb atoms and is designated as (111)*B*. These two surfaces exhibit striking differences in their chemical, electrical and mechanical properties.

From high pressure Raman studies at 300 K, it has been found that above 7.65 GPa, a white tin structure with space group $D_{4h}^{19} - I(4_{1/a})md$ result.^[25]

2.2 Thermal properties



2.2.1 Heat capacity and Debye temperature

Very few measurements of heat capacity are available in the literature for GaSb. Piesbergen^[26] measured the value of c_p, c_v and θ for GaSb in the temperature range of 12-273K. For temperature in the range 20-700 °C, c_p can be expressed as:^[27]

$$c_p = 0.04351 + (4.635 \times 10^{-5} T) \text{ cal/g deg.} \quad (2.2)$$

where T is the temperature in °C.

The value of c_p at 298K is 0.06858 cal/g deg. The temperature dependence of specific heat c_v is shown in Fig. 2.1.^[28] The plot of Debye temperature (θ) versus temperature is shown in Fig. 2.2. As can be seen from the figure, the θ runs through a minimum at low temperatures. This minimum is in agreement with the results from the lattice absorption band in the infrared, which give a relatively low energy

for the transverse acoustic phonons.^[29,30] The decrease in θ at higher temperatures is believed to be due to anharmonic effects in the lattice vibrations. In order to give an estimate of this contribution, a parameter θ_∞ is calculated from Thirring expansion, this value for GaSb is 316K. At very low temperatures, where only the low frequencies contribute to atomic heat, the value of θ is calculated to be 266K.^[31-33]

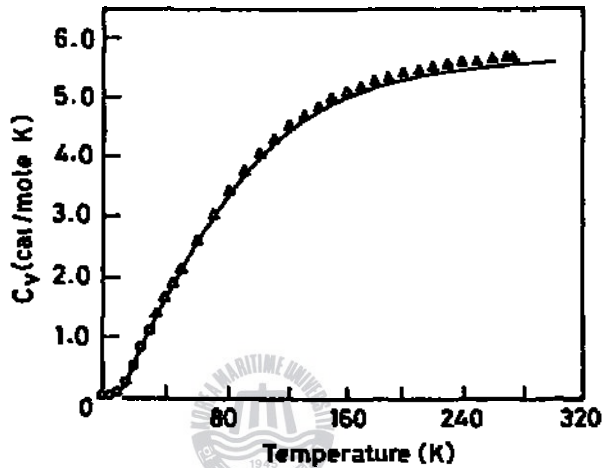


Fig. 2.1 Comparison of heat capacity of GaSb calculated from $g(\nu)$ with the experimental data^[28].

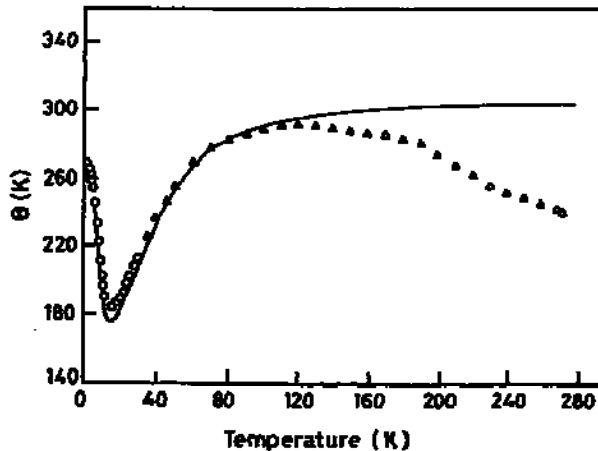


Fig. 2.2 Comparison of the Debye temperature for GaSb calculated from $g(\nu)$ with experiment data^[28].

2.2.2 Elastic moduli and phonon dispersion

The measurements of the elastic properties of the III–V compounds have so far been mainly confined to the determination of the three second-order constants. The second-order elastic moduli versus temperature plots for GaSb obtained using ultrasonic technique^[34] are shown in Fig. 2.3. The values of elastic moduli, c_{11} , c_{44} and c_{12} (in 10^{11} dyn cm⁻²) at 296 K are 8.834, 4.322 and 4.023, respectively.

The phonon dispersion relations are shown in Fig. 2.4. The experimental points are obtained from inelastic neutron scattering experiments.^[35] The continuous curves are obtained from the parameter shell model calculation. From first-order^[25] and second-order^[36] Raman scattering experiments at 300 K, the phonon wave numbers (in cm⁻¹) obtained are indicated below

$$\begin{aligned} \overline{\nu_{TO}}(\Gamma) : 223.6, \overline{\nu_{LO}}(\Gamma) : 232.6, \\ \overline{\nu_{TA}}(L) : 46, \overline{\nu_{TA}}(X) : 56, \\ \overline{\nu_{TA}}(W) : 75, \overline{\nu_{LA}}(L) : 155, \\ \overline{\nu_{LO}}(L) : 204, \overline{\nu_{LO}}(X) : 210, \\ \overline{\nu_{TO}}(\Gamma, X, \Sigma) : 218. \end{aligned}$$

Fig. 2.5 shows the Raman spectra of GaSb taken for the 5309 Å line at various pressures.^[25] With increasing pressure, the LO and TO phonons shift to higher frequencies and their peak heights also vary. The intensities of phonon peaks increase with pressure, go through a maximum and then decrease. The transition to the metallic phase occurs at 7.65 GPa. The shifts of the phonon frequencies with relative lattice constant ($-\Delta a/a$) and pressure are shown in Fig. 2.6.

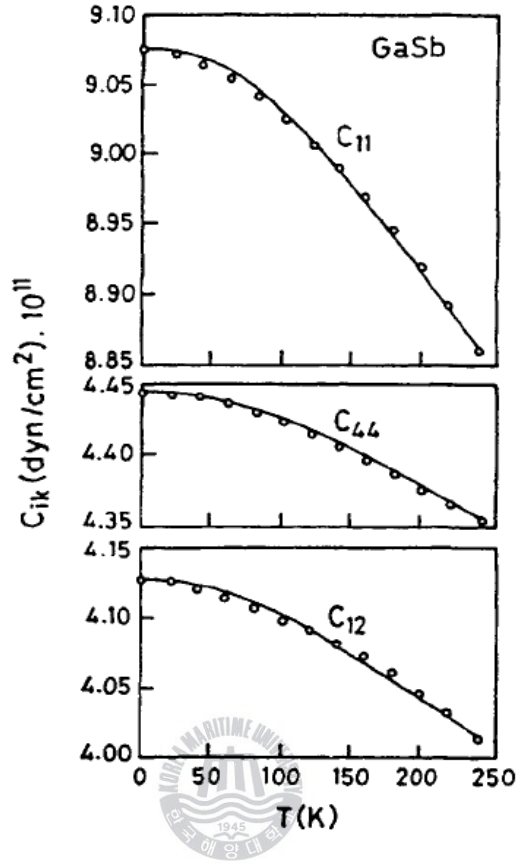


Fig. 2.3 Temperature dependence of second-order elastic moduli^[34].

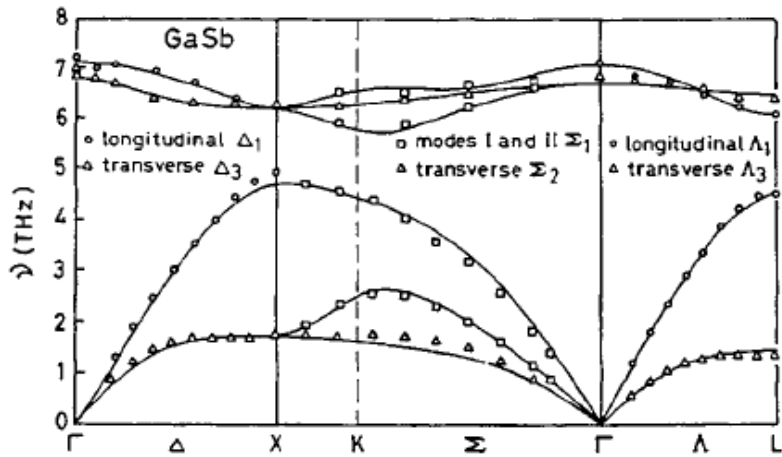


Fig. 2.4 Phonon dispersion relation for GaSb. Symbol: experimental data; continuous lines: calculation^[35].

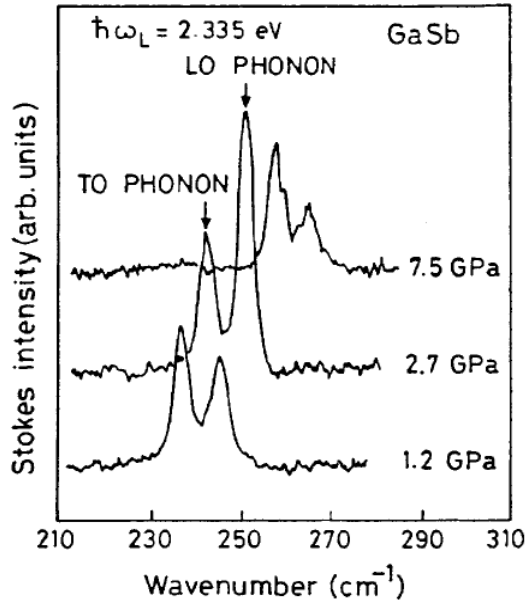


Fig. 2.5 First-order Stokes Raman spectra for GaSb taken with the 5309Å laser line at different pressure^[25].

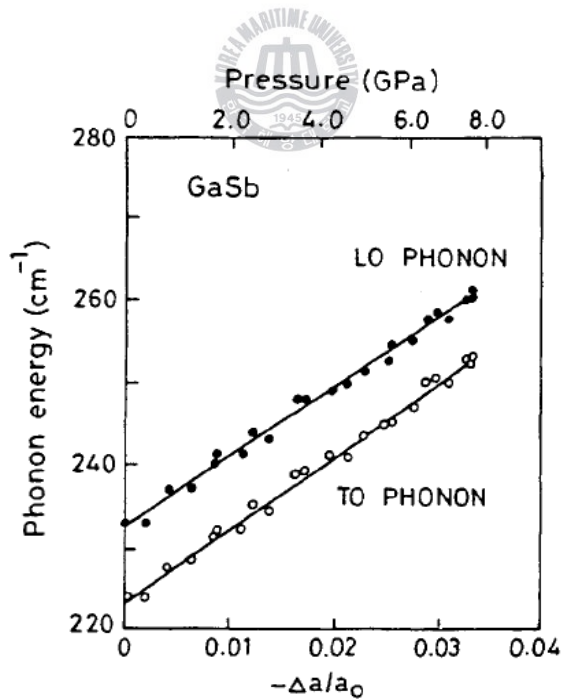


Fig. 2.6 Dependence of the TO and LO phonon frequencies of GaSb on linear lattice compression (lower scale) and pressure (upper scale). Solid lines are least squares fits to the experimental data^[25].

2.2.3 Thermal expansion

The linear thermal expansion coefficient α for GaSb in the temperature range 25–340 K is shown in Fig. 2.7.^[37] As can be seen from the figure, α is negative for temperatures less than 0.2θ . For cubic structures, the volume coefficient of thermal expansion β is equal to α .

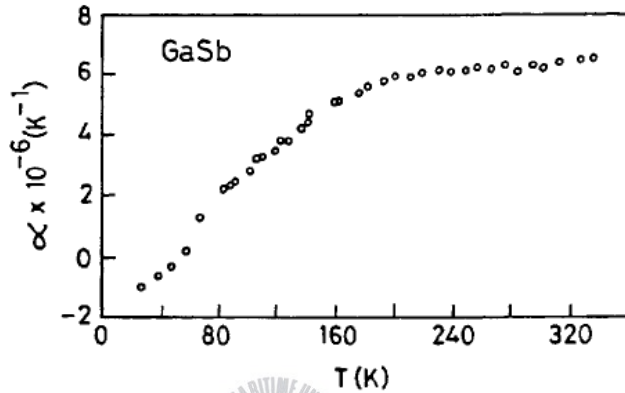


Fig. 2.7 Temperature dependence of linear thermal expansion coefficient of GaSb from 4.2 to 340 K^[37].

The thermal expansion of GaSb above room temperature has been investigated by Bernstein and Beals.^[38] The temperature dependence of the relative expansion is shown in Fig. 2.8. As can be seen from the figure, a sharp deviation from linearity is observed in the interval 300–400 °C, and it was impossible to make measurements beyond 436 °C.

The temperature dependence of Gruneisen parameter γ for GaSb is shown in Fig. 2.9.^[39] Near the Debye temperature γ is independent of temperature. At low temperatures γ has a region of negative values which coincides with the region in which the expansion coefficient is negative. The temperature at which γ changes sign coincides with the temperature at which α also changes sign.

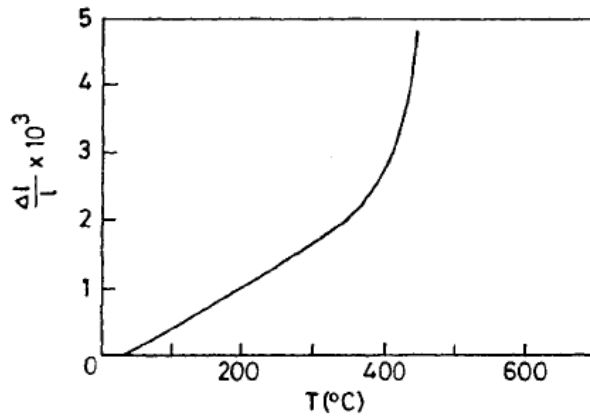


Fig. 2.8 Temperature dependence of linear thermal expansion coefficient of GaSb above room temperature ^[38].

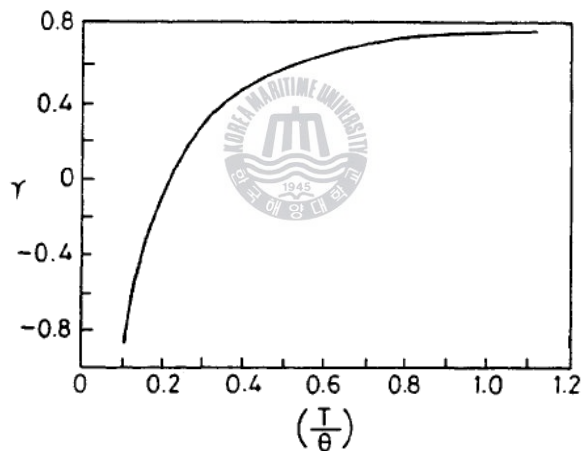


Fig. 2.9 Temperature dependence of Grüneisen parameter for GaSb ^[39].

2.2.4 Thermal conductivity

The thermal conductivity as a function of temperature for four GaSb samples (p and n type) is shown in Fig. 2.10. ^[40,41] The shape of the curves is similar to that obtained theoretically for III–V compounds by considering the contributions from various scattering processes like crystalline boundaries, impurities, three-phonon, four-phonon, resonance and electron–phonon scattering; however, it should be

noted that the experimental data showed a change in slope at low temperatures for the p -type samples. As can be seen from the figure, even though the n -type samples contain 10 times more impurity than the p -type samples, they possess a higher value of k for most of the low temperature region. Theoretically calculated thermal conductivity at low temperatures (up to 10 K) in the boundary scattering region overestimates the experimental data by almost a factor of 100. An attempt was made to fit the data using an analysis due to Ziman^[42] which treats scattering of phonons by electrons in a degenerate band. While the magnitude of the thermal conductivity is correctly predicted, this scattering does not account for the change in slope in the p -type material nor can it account for the dependence on impurity concentration. Further, by using the electron–phonon mechanism suggested by Keyes,^[43] an attempt was made to fit the data.^[44] In this case, the scattering is due to the strain sensitivity of the donor (or acceptor) ground-state energy. The change in slope near 5K could be obtained in the analysis.

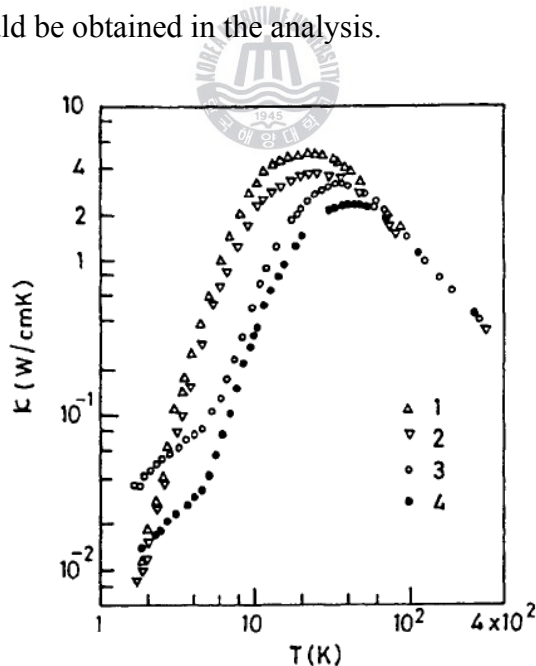


Fig. 2.10 Thermal conductivity of GaSb for n - and p -type samples. (1) $n= 4 \times 10^{18} \text{ cm}^{-3}$, (2) $n = 1.4 \times 10^{18} \text{ cm}^{-3}$, (3) $p= 1 \times 10^{17} \text{ cm}^{-3}$, (4) $p=2 \times 10^{17} \text{ cm}^{-3}$ [41].

The high temperature lattice thermal conductivity of GaSb is shown in Fig. 2.11.^[45] The decrease in κ with increasing free carrier concentration is attributed to scattering of phonons by electrons. Some optical phonon scattering has also been identified. Steigmeier and Kudman^[45,46] have evaluated the influence of optical mode scattering on the lattice thermal conductivity of group IV and III–V semiconductors. Using the values of $M1/M2$, M , θ and κ , they calculated the Gruneisen anharmonicity parameter. The values of each of these quantities for GaSb are listed below.

$M1 / M2$ (Atomic mass ratio): 1.75,

M (Mean atomic mass): 95.7,

θ (Debye temperature in K): 265.5,

κ (at 300 K in W/cm deg): 0.390,

γ (at $T=\theta$): 0.86.

The large value of γ for GaSb implies significant scattering by the optical mode. The thermal conductivity of GaSb has also been investigated in the presence of magnetic field in the low temperature region, however it has been found to be independent of the magnetic field.^[28]

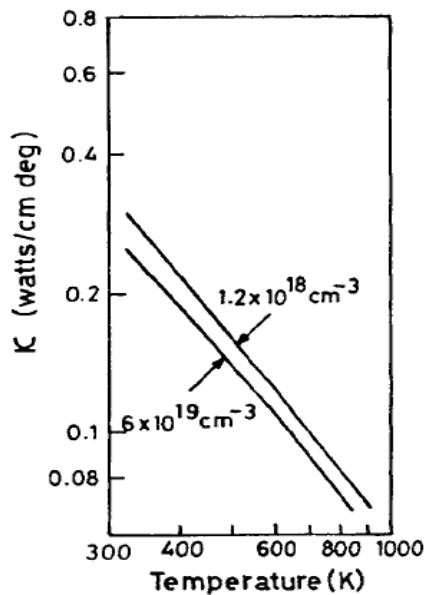


Fig. 2.11 High temperature thermal conductivity of GaSb^[45].

2.3 Electronic and transport properties

2.3.1 Band structure

Fig. 2.12 shows the band structure of GaSb obtained with a nonlocal pseudopotential calculation.^[47] The symmetry symbols are in double group notation. The conduction band is characterized by three sets of minima. The lowest minimum is at Γ . The next higher minima are the L points at the surface of the Brillouin zone and at the X points. The valence band has the structure common to all zinc-blende semiconductors. The energies of the symmetry points of the band structure relative to the top of the valence band (in eV) are given in Table 2.1. The first column gives the theoretically calculated values, the second column is obtained from the angle resolved photoelectron spectroscopy experiment (ARPES) at 300 K^[48] and the third column is the electroreflectance data (EL) at 10K.^[49]

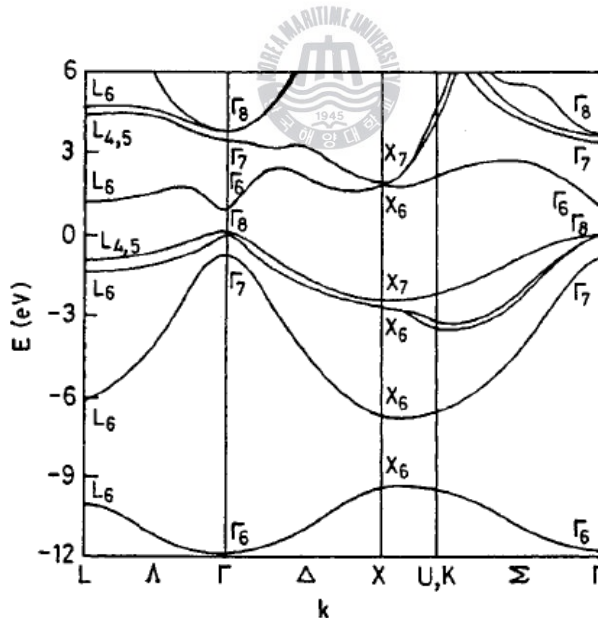


Fig. 2.12 Band structure of GaSb^[47].

Table 2.1 Energies of symmetry points of band structure relative to the top of valence band (in eV)^[47-49].

Symmetry points	Theory	APRES	EL
$E(\Gamma_{6v})$	-12.00	-11.64	
$E(\Gamma_{7v})$	-0.76	-0.82	-0.756
$E(\Gamma_{8v})$	0		
$E(\Gamma_{6c})$	0.86		0.822
$E(\Gamma_{7c})$	3.44		3.191
$E(\Gamma_{8c})$	3.77		3.404
$E(\Gamma_{8c})$			7.9
$E(L_{6v})$	-10.17	-10.06	
$E(L_{6v})$	-6.25	-6.60	
$E(L_{6v})$	-1.45	-1.55	-1.530
$E(L_{4,5v})$	-1.00	-1.10	
$E(L_{6c})$	1.22		1.095
$E(L_{4,5c})$	4.43		4.36
$E(L_{6c})$	4.59		4.49
$E(X_{6v})$	-9.33	-9.62	
$E(X_{6v})$	-6.76	-6.90	
$E(X_{6v})$	-2.61	-3.10	
$E(X_{7v})$	-2.37	-2.86	
$E(X_{6c})$	1.72		
$E(X_{7c})$	1.79		
$E(\Sigma_{3,4v}^{\min})$		-3.64	
		-3.90	

Using photoluminescence spectroscopy^[50] at 2 K, the excitonic gap E_{gx} has been found to be 0.8099 eV. Assuming an exciton binding energy of 1.4 meV, the direct band gap $E_{g,dir} (\Gamma_{8v} - \Gamma_{6c})$ was evaluated to be 0.8113 eV. The extrapolated band gap at 0 K was found to be 0.822 eV from the electroreflectance experiment^[51] as shown in Fig. 2.13. The band gap at 300 K is 0.725 eV. The values of constants α and β used in the equation for evaluating the band gap at various temperatures from the band gap at 0 K are $4.2 \times 10^{-4} \text{ eV K}^{-1}$ and 140, respectively.

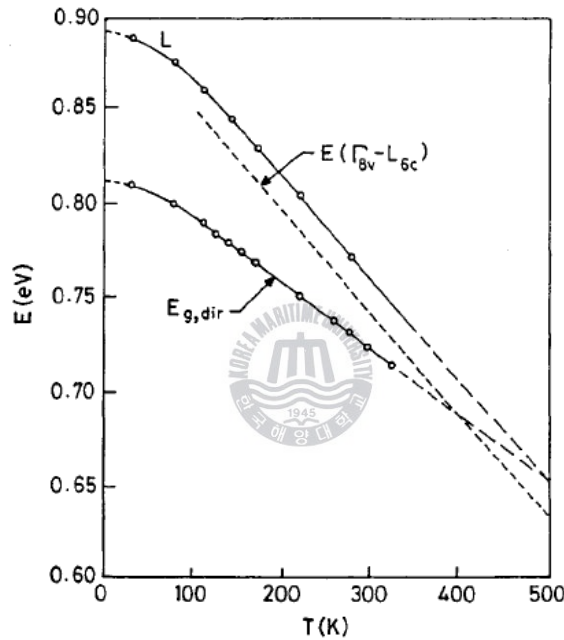


Fig. 2.13 Energies of electroreflectance peaks as a function of temperature^[51].

The direct gap energies calculated from interband direct Faraday rotation are 0.74 and 0.82 eV at 296 and 77 K, respectively.^[52]

The pressure dependence of the absorption edge is given below:

$$\frac{dE_g}{dP} = 12 \times 10^{-6} \text{ eV/kg/cm}^2 \text{ for } P \leq 18000 \text{ kg/cm}^2$$

$$\frac{dE_g}{dP} = 7.3 \times 10^{-6} \text{ eV/kg/cm}^2$$

for $18000 \text{ kg/cm}^2 \leq P \leq 45000 \text{ kg/cm}^2$,

$$\frac{dE_g}{dP} = \text{negative for } P \geq 45000 \text{ kg/cm}^2$$

At normal pressures, the (000) band lies lowest, followed by the (111) and then (100) bands. The minima assigned to the above three pressure ranges are (000), (111) and (100), respectively.

The critical point and spin-orbit splitting energies (in eV) as measured from modulation spectroscopy^[53] at 27 K are given below

$$\begin{aligned} E_0 + \Delta_0 &= (\Gamma_{7v} - \Gamma_{6c}) = 1.569, \\ E_1 &= (\Gamma_{4,5v} - \Gamma_{6c}) = 2.185, \\ E_1 + \Delta_1 &= (\Gamma_{6v} - \Gamma_{6c}) = 2.622, \\ E_L &= (\Gamma_{8v} - \Gamma_{6c}) = 0.871. \end{aligned}$$

The intraconduction band energy difference between the lowest conduction band minimum (Γ_{6c}) and the lowest L band minimum (L_{6c}) was found to be 61 and 82 meV at 300 K employing Hall and magnetoresistance measurements.^[54] The two values have been obtained by assuming the effective mass of electron in L band to be $0.22m_0$ and $0.43m_0$, respectively. The energy difference between the Γ -band minimum and the X -band minimum was found to be 430 meV at 10 K using the electroreflectance technique.^[49]

The camel's back structure of conduction band edge was estimated from the $k \cdot p$ theory using the GaP data.^[55] The values of various camel's back parameters are tabulated below

$$\Delta: 178 \text{ meV},$$

$$\Delta E: 25.1 \text{ meV},$$

$$k_m: 0.127(2\pi/a),$$

$$m_t: 0.250m_0,$$

$$m_{\parallel}: 1.2m_0.$$

The electron g factor at 30 K calculated using stress modulated magnetorefectance has been evaluated to be -7.8.^[56]

Molar magnetic susceptibility as a function of temperature in the range of 4.2–900 K has been evaluated and found to lie in between -40 and -38 cm³/mol.^[52]

The energy–wave-vector relation for holes in III–V compounds, including GaSb, contains a linear- k term owing to lack of inversion symmetry in their crystal structure, by the spin-orbit splitting. As shown by Dresselhaus, Kip, and Kittel^[57] because of the linear- k term, the light and heavy hole bands are split into two nondegenerate bands, and the energy maxima of the valence bands are not at $k(0,0,0)$. The maxima of the heavy hole bands are shifted in [111] direction and that of the light hole bands in [100] direction. From an analysis of transport data the following values for the difference of energies at the top of the bands and at $k = 0$ have been found.^[58,59]

$$\Delta E[111]: 20 \text{ meV}; \Delta E[111]: 5 \text{ meV};$$

$$\Delta E[111] - \Delta E[100]: 7.5 \text{ meV}.$$

The influence of the linear- k term on the shape of the isoenergetic surfaces in p -GaSb has been deduced by Robert *et al.*^[60] from galvanometric measurements. They have shown that the nonquadratic band model employed for Ge and Si is insufficient to account for all the observed galvanometric phenomena. They

determined the anisotropy coefficients of the light and heavy hole ellipsoids along the [100] and [111] directions to be 1.66 and 3, respectively.

The valence band parameters A , B and C used in the nonquadratic $E - k$ relation calculated using $k \cdot p$ theory^[61] are 11.7, 8.19 and 11.07, respectively. From cyclotron resonance measurements on p -GaSb in the range 12–20 K, Stradling^[62] determined these values to be 11 ± 0.6 , 6 ± 1.5 and 11 ± 4 , respectively, which are in good agreement with the theoretically predicted values.

2.3.2 Effective masses of electrons and holes

The effective masses of electrons and holes have been evaluated by cyclotron resonance technique and from the density of state analysis of transport data.^[63,64] In Table 2.2, the effective masses for electrons (m_e) in the Γ , L and X conduction bands and that for holes (m_p) in heavy and light hole valence bands along with the density of state masses are listed.

The density of state effective mass obtained from electron concentration (transport) measurements can be different from that obtained from reflection measurements.^[52] The difference is due to the anisotropy of the upper subband. High resolution magneto-absorption measurements made at photon energies just above the intrinsic absorption edge in GaSb have revealed an oscillatory spectrum. The value of the energy gap found is

$$E_g = 0.813 \pm 0.001 \text{ eV and electron effective mass, } m^* = (0.47 \pm 0.003)m_0. \text{ [52]}$$

The optically determined hole mass is considerably smaller than the one derived from electrical measurements.

Due to close proximity of the L band to the conduction band minimum, appreciable population of electrons exists in the L band above room temperature. Since the effective mass of electron is more in the L band, it will affect the electron

mobility above room temperature. Moreover, for Schottky diodes the Richardson constant (and hence the barrier height) will also get affected by the population of electrons in the L band.

Table 2.2 Effective masses of electrons and holes (in terms of free electron mass, m_0)^[66,67]

Notation	Numerical Value	Remarks
$m_e(\Gamma)$	0.0412	From cyclotron resonance of hot electrons in the temperature range of 1-30K
$m_e(\Gamma)$	0.0396	Same data as above but by taking into account the nonparabolicity and polaron effect
$m_e(L)_\perp$	0.11	From transverse conductivity
$m_e(L)_\parallel$	0.95	From longitudinal conductivity
$m_{de}(L)$	0.226	Density of state mass
$m_e(X)_\perp$	0.22	From transverse conductivity
$m_e(X)_\parallel$	0.51	From longitudinal conductivity
$m_p(h)$	0.28	From conductivity data
$m_p(l)$	0.05	From conductivity data
m_{dp}	0.82	Density of state mass

2.3.3 Electron transport

The transport properties of GaSb have been the subject of investigation for the past 3 decades.^[65-82] This is because of some special features of its band structure. Transport in *n*-type GaSb is complicated due to the contributions from Γ , *L* and *X* conduction bands. Experimental data on transport coefficients can be consistently explained by a three band model,^[64] the *X* bands contributing to transport above 180 °C. The room temperature electron mobility (in cm²/Vs) for a sample with $n = 1.49 \times 10^{18}$ cm⁻³ was found to be 3750, 482 and 107 at the *G*-, *L*- and *X*-band minima, respectively. Furthermore, for the *L*-band at room temperature, the mobility was found to be 500–800 and 800–1600 cm²/Vs at 120K.^[53] Fig. 2.14 shows the temperature dependence and the contributions of various scattering mechanisms to the electron mobility.^[64]

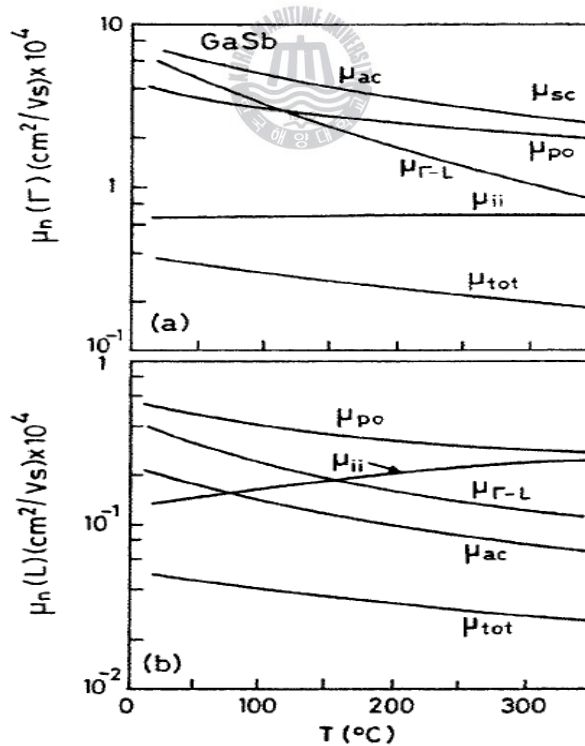


Fig. 2.14 Temperature dependence of electron mobility in Γ and *L* band for GaSb with $n = 1.49 \times 10^{18}$ cm⁻³^[64].

Sagar^[66] discussed the results of Hall coefficient measurements on *n*-type material on the basis of the two-band model. The purer samples have higher Hall coefficient at any given temperature. The special features are the increasing Hall coefficient with increasing temperature for the pure samples and the appearance of a maximum for the heavier doped crystals. Since the effective mass at the (000) Minima is smaller than that at the (111) minima, for a constant total number of electrons, an increasing Hall coefficient with increasing occupation ratio n_2/n_1 , i.e., with increasing temperature, is observed. A maximum is reached when the total number of electrons starts to increase at the onset of the intrinsic region, since then R_H drops rapidly. Measurements by Strauss^[67] show a characteristic difference in the doping dependence of the Hall coefficient for Se- and Te-doped samples. The difference is most pronounced at heavy doping and disappears for very pure samples. One possible interpretation is that impurity-band conduction is dominating in this region, and that this depends on the nature of the donor. The two subbands of the conduction band of GaSb both contribute strongly to the magnetoresistance. In purer samples, the magnetoresistance decreases with decreasing temperature, whereas in heavily doped samples, the opposite trend is observed. The influence of the second band becomes noticeable as soon as the electron concentration surpasses the value of $1.25 \times 10^{18} \text{ cm}^{-3}$. Pressure dependence of the resistance, Hall coefficient and the thermoelectric power confirmed the presence of three subbands in the conduction band. The third subband appears only at 25000 kg/cm^2 . From the Z coefficients (piezoresistance) measurements under hydrostatic pressure, the (000) subband has been found to displace upward relative to the (111) subband with increasing pressure. Its contribution to the conductivity therefore decreases. Since the density of state in the (000) band is considerably smaller than in the (111) band, there are only few electrons in the (000) band; however, they contribute considerably to the conductivity because of their high mobility. When these electrons are brought into the (111) band by pressure, their

small number does not add much to the contribution of this subband to the conductivity and piezoresistance. From thermoelectric power measurements on *p*-GaSb in the temperature region from 280K to above the melting point the effective mass of the holes has been found to strongly depend on temperature and to be doping dependent. An abrupt change of the thermoelectric power is observed at the melting point.

In GaSb, the donor states below the (000) minimum fuse into the conduction band; the ones lying below the (111) minima, however, keep a finite ionization energy because of the larger effective mass of the electrons in these minima. These discrete impurity levels lie a few hundredths of an eV below the (111) minima but still above the (000) conduction band at constant energy. Thus the separation of the impurity levels from the (111) conduction band is not a true ionization energy that must be overcome to make the donor electrons electrically active. The only property of these states is that they are empty at low electron concentration and filled at high concentration. In the first case they act as charged impurities, in the second as neutral ones. This can cause anomalies in the dependence of the electron mobility on the electron concentration. This model can explain the differences between the electrical properties of Se- and Te-doped GaSb.

The pressure variation of the resistivity of S-, Se- and Te-doped (*n*-type) GaSb has been studied to 50 kbar. All three types exhibit saturation in resistivity at the highest pressures attained, although the resistivity of S- and Se-doped samples increases several orders of magnitude before saturation, in contrast to Te-doped samples, whose resistivity increases only by a factor of 14. The saturation in resistivity is due to the X_1 minima becoming the lowest conduction band edge at these pressures.

Even though numerous investigators have explained their Hall data on *n*-GaSb by considering the effects of relatively low lying *L* and *X* conduction

bands,^[66] there are, however, some peculiarities in the electrical properties of *n*-GaSb occurring at lower doping levels which do not appear to be the result of multiple-band conduction. For example, the mobility at low temperatures is observed to increase monotonically with increasing electron concentration for Te-doped GaSb.^[67] Also, the diffusion of lithium into Te-doped material has resulted in significant increase in electron mobilities coupled with modest increase in electron concentration.^[68,69] Long and Hager,^[70] in their investigation of near resonance scattering in GaSb at low temperatures, pointed out the basic importance of compensation in regard to the observed increase in mobility with electron concentration. This behavior is in contrast to that found in *n*-type GaAs and InAs, where compensation is significantly lower.^[71] Later, Baxter and co-workers^[72] illustrated the effect of compensation on Coulomb scattering from the well known Brooks–Herring treatment.^[73] The ionized impurity mobility is in general an increasing function of carrier concentration n and inversely proportional to N_I , the ionized impurity concentration. In the absence of compensation, N_I is equal to n ; however, with high concentration of compensating centers, N_I varies much more slowly with n and the variation of mobility is entirely controlled through n . Further, to fit the mobility data for low electron concentrations the required hole concentration is 2–3 times more than that observed in undoped GaSb.^[72] Baxter and co-workers^[72] have explained this with the double ionizable nature of the native defect. The higher hole concentration needed to fit the data arises from a deep lying acceptor level which is not appreciably ionized at room temperature in the undoped samples. Such a level would, of course, be completely ionized in *n*-type material and account for the apparently high estimates for the compensating acceptors. Several workers have adopted the approach of compensating the crystals with Te to shift the Fermi level toward the conduction band and hence observe the deeper level; but, as evidenced from luminescence measurements^[74] and pointed out by Johnson and co-workers,^[75] incorporation of donor dopant Te is

accompanied by the formation of an additional acceptor state near the singly ionized state of the native defect, which is often confused with the energy levels of the native acceptor.^[76-80] This would also explain the high estimates for the compensating acceptors. Shubnikov–de Haas oscillations have been observed in Te-doped GaSb diffused with lithium as shown in Fig. 2.15^[81] The oscillation has been attributed to electron population in the *L* band.^[81] Recently, we have studied the hole transport properties of undoped and tellurium compensated *p*-GaSb in the temperature range of 4.2–300 K with an aim to clarify these anomalies, paying special attention to the behavior of the deeper energy levels. This aspect is discussed below.

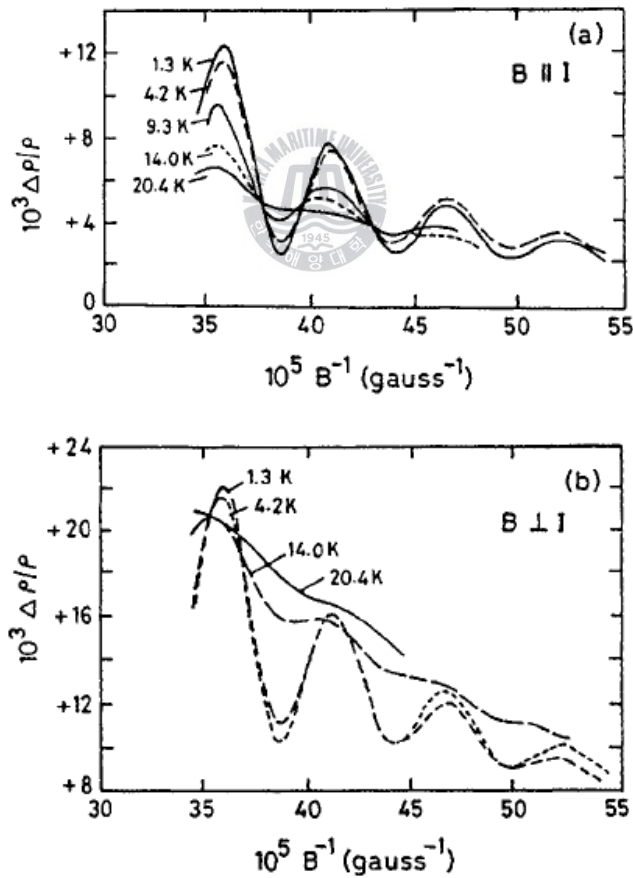


Fig. 2.15 (a) Transverse and (b) longitudinal magnetoresistance oscillations at various temperatures for Te-doped n-GaSb samples after Li diffusion^[81].

2.3.4 Hole transport

In *p*-type III–V compounds, the dominant factors limiting mobility have been found to be acoustic, nonpolar and polar optical phonons and ionized impurity scatterings.^[61,82] In *p*-GaSb, owing to the close proximity of the heavy and light hole bands, intervalley and intravalley scatterings occur. Thus, the contributions from both the light hole and heavy hole bands to various transport properties should be taken into account.^[57,58] The hole transport properties at low temperatures can be explained consistently by the multiellipsoidal model to take into account the shift of the heavy and light hole bands away from $k=0$, whereas at high temperatures a warped sphere model (as in Si and Ge) is adequate.^[57,58] Analyses of transport data between 77 and 300 K have to take into account the intermediate region between the two limiting cases in which the effective mass of heavy holes varies with temperature as shown in Fig. 2.16^[83] Fig. 2.17 shows the temperature dependence of mobility along with the contributions of heavy and light holes without taking into account of the variation of heavy hole effective mass with temperature.^[57]

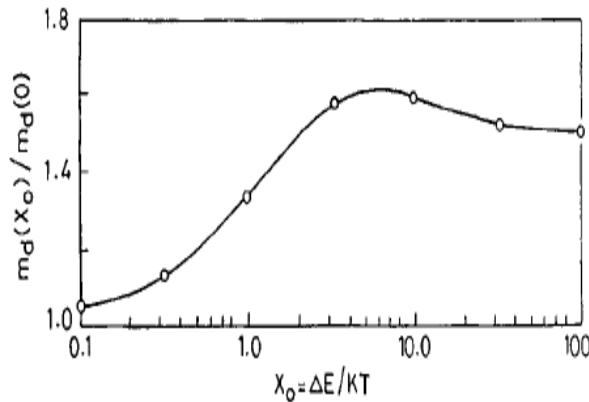


Fig. 2.16 Heavy hole density of states effective mass as a function of reciprocal temperature^[83].

By taking into account the temperature dependence of heavy hole density of states effective mass, we have investigated the transport properties of undoped and

Te compensated p -GaSb with the knowledge of defect levels from luminescence studies.⁸⁴

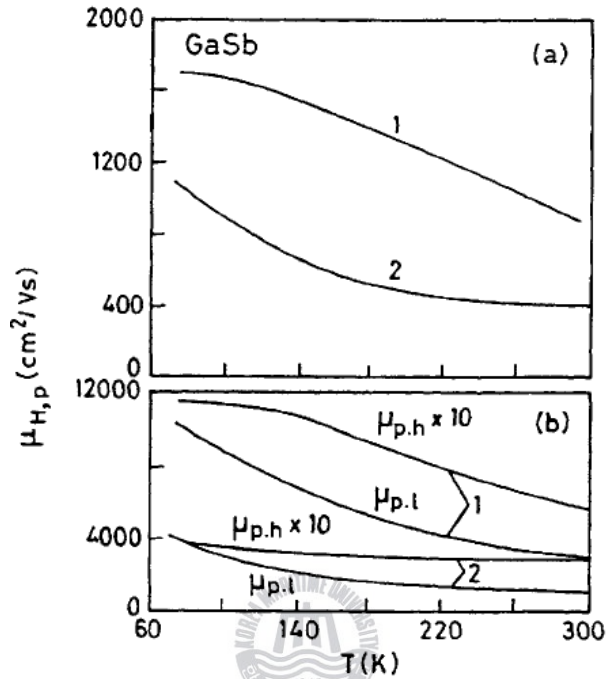


Fig. 2.17 Hole mobility as a function of temperature: (a) for two samples (1) $8 \times 10^{17} \text{ cm}^{-3}$, (2) $3 \times 10^{18} \text{ cm}^{-3}$; (b) contributions from heavy (h) and light (l) holes^[57].

Evidence for *self-compensation* is seen on Te doping by the formation of a Te-related acceptor complex. Excellent agreement between the theoretically calculated and experimentally measured mobilities has been obtained, by including the Te-related acceptor $V_{\text{Ga}}\text{Ga}_{\text{Sb}}\text{Te}_{\text{Sb}}$ apart from the doubly ionizable native defect $V_{\text{Ga}}\text{Ga}_{\text{Sb}}$. The mobility as a function of temperature for undoped samples grown from stoichiometric and constoichiometric melts along with Te compensated samples to various degrees are shown in Fig. 2.18.

As depicted in Fig. 2.18, with increase in Te concentration the mobility decreases and a shift in the mobility peak to higher temperature is observed. The partial mobilities for various scattering mechanisms along with the total mobility

for the undoped and Te compensated samples are shown in Figs. 2.19 and 2.20, respectively. At low temperatures, the largest contribution to hole scattering comes from ionized impurities for both the samples. At room temperature nonpolar and polar optical phonons and acoustic scatterings all make significant contributions for the undoped sample, whereas ionized impurity scattering is still dominant for the Te compensated sample.

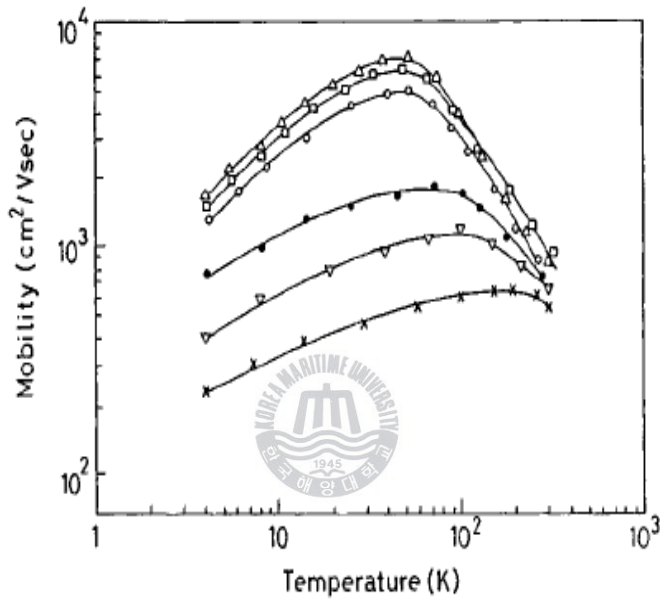


Fig. 2.18 Hole mobility as a function of temperature for (\circ) undoped p -GaSb grown from stoichiometric melt, (\square) undoped p -GaSb grown from Ga-rich melt, (Δ) undoped p -GaSb grown from Sb-rich melt, and (\bullet, ∇, \times) Te-compensated p -GaSb to various degrees^[84].

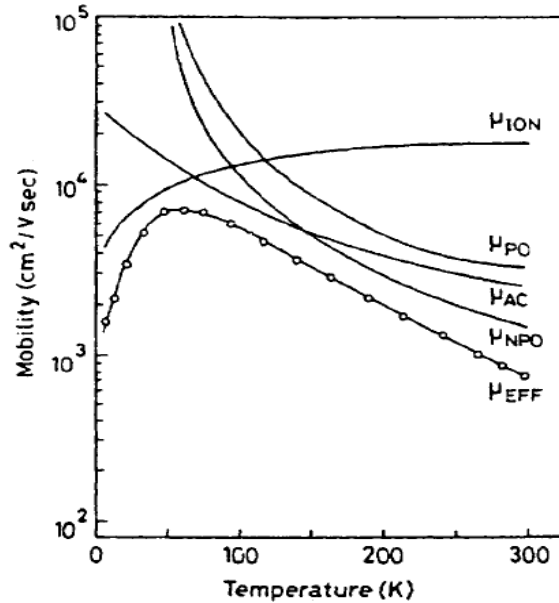


Fig. 2.19 Temperature variation of theoretically calculated partial mobilities and effective mobility (solid curves) for undoped p -GaSb. The experimental data are represented by (○) [84].

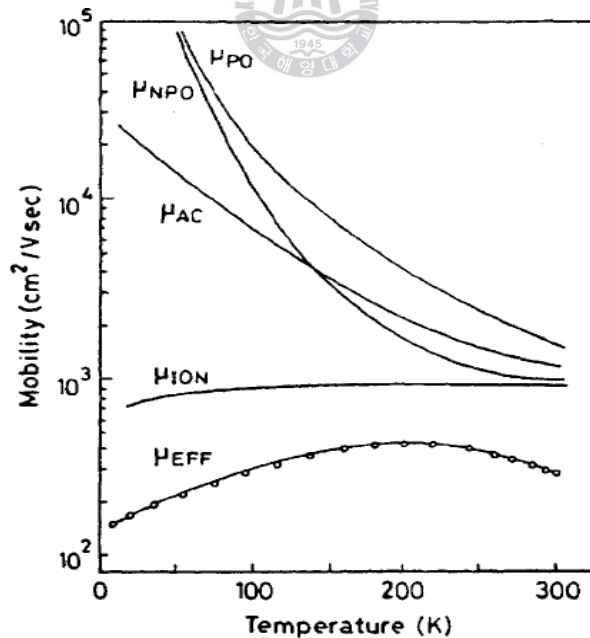


Fig. 2.20 Temperature variation of theoretically calculated partial mobilities and effective mobility (solid curves) for a typical heavily Te-compensated p -GaSb. The experimental data are represented by (○) [84].

Johnson *et al.*^[85] have also studied the effect of compensation in MBE grown *p*-type GaSb epilayers by varying the Sb/Ga ratio in the flux. They found that the layers with the lowest residual acceptor concentrations are not those that display the highest hole mobility, confirming the effect of compensation.

Fig. 2.21 shows the intrinsic carrier concentration as a function of temperature. As can be seen, GaSb achieves an intrinsic carrier concentration of $n_i \approx 10^{17} \text{ cm}^{-3}$ in the neighbourhood of 600 K.^[86] The temperature dependence of mobility above room temperature for a typical sample with $N_A \approx 10^{17} \text{ cm}^{-3}$ is shown in Fig. 2.22. At a temperature of approximately 630 K, the sample converts from *p* to *n* type due to rapidly increasing intrinsic carrier concentration and the larger mobility of the electrons. The exact temperature at which this conversion takes place depends, among other things, on the acceptor concentration and is lower for lower densities of acceptors. For GaSb there is no exhaustion region where the electron population of the impurities remains constant while the Fermi level varies with temperature. Hence the employment of data from luminescence experiments is all the more essential to interpret the Hall data accurately and reliably.

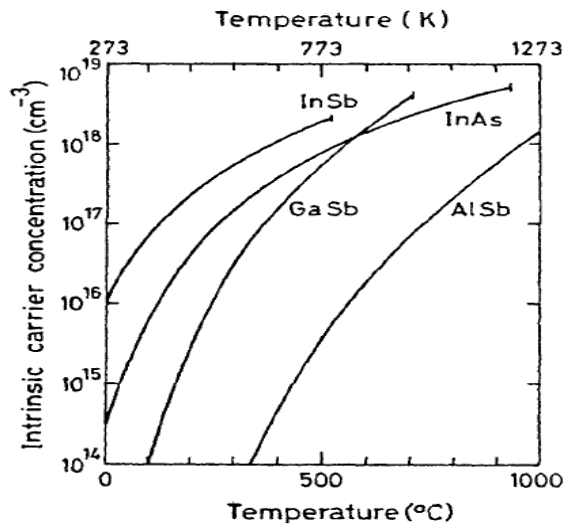


Fig. 2.21 Plot of intrinsic carrier concentration as a function of temperature for undoped *p*-GaSb^[86].

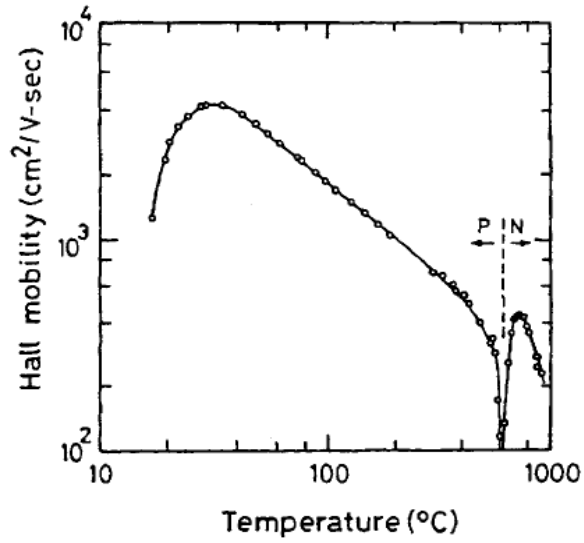


Fig. 2.22 Mobility as a function of temperature for undoped p -GaSb above room temperature^[86].

Some of the important material properties of GaSb are listed in Table 2.3^[5].



Table 2.3 The important material properties of GaSb.

Lattice constant (Å)	6.0959
Density (gm cm ⁻³)	5.6137
Melting point (K)	985
Debye temperature(K)	266
Coefficient of thermal expansion (10 ⁻⁶ °C ⁻¹) (at 300K)	7.75
Thermal conductivity at 300K (W cm ⁻¹ K ⁻¹)	0.39
Direct energy gap at 300K (eV)	0.725
Direct energy gap at 0K (eV)	0.822
Temperature dependence of minimum energy gap (x 10 ⁻⁴ eVK ⁻¹) α	4.2
β	140
Spin-orbit splitting energy, Δ_0 (eV)	0.8
Effective mass of electrons (in unit of m_0)	0.042
Effective mass of holes (in unit of m_0)	
Heavy hole mass	0.28
Light hole mass	0.05
Spin-orbit split mass	0.13
Wave number of LO phonons (cm ⁻¹)	233.0
Wave number of TO phonons (cm ⁻¹)	224.0
Refractive index (near band-gap energy)	3.82
Dielectric constant	
ϵ_0	15.69
ϵ_∞	14.44
Elastic compliances (x10 ⁻¹² cm ² dyn ⁻¹)	
S11	1.582
S12	-0.495
S14	2.314
Deformation potential constants	
a (eV) (for direct gap)	-8.28
b (eV)	-2.0
c (eV)	-4.7

Chapter 3 Growth of GaSb:Te epilayers on GaAs (001) substrate

3.1 Introduction

The main difficulty in growing GaSb by MBE is again the low vapour pressure of antimony.^[87] As a result, during crystal growth Sb will have a low surface mobility and tend to aggregate together forming clusters and precipitates. This leads to vacant Sb sites. Thus, antisite defects like Ga_{Sb} are formed. Therefore, to improve the quality of MBE grown layers, an Sb-rich environment is needed. One can achieve this by using proper orientation of the substrate like (311)*B*, (111)*B*, etc. Longenbach and Wang^[88] used (311)*B* oriented substrates to reduce the native *p*-type centres in the grown layers. Usually the growth rate varied from 0.6 to 2.5 mm/h for the growth temperatures in the range of 500–600°C. Very low acceptor concentration ($\approx 10^{15} \text{ cm}^{-3}$) could be obtained using this approach. Undoped GaSb epilayers have shown C and O impurities. The origin of these impurities can vary from one growth system to another and can be due to different sources.

Generally, Te doping is accomplished in MBE grown layers by the use of a PbTe^[89] cell since this provides better control of temperature than the use of elemental Te. There appears to be a trace incorporation of Pb in the grown layer. Donor concentrations of above 10^{18} cm^{-3} are readily obtained. Other compounds that may be used for Te doping are GaTe, SbTe, GeTe and SnTe^[90-94].

3.1.1 Zinc Telluride (ZnTe) buffer layer

Epitaxial layers grown between the substrate and the active epitaxial device layers are known as buffer layers. Buffer layers serve several purposes, including: (i) moving the device active regions away from the substrate/epitaxial interface to minimize the undesirable effects caused by surface damage and contamination

(introduced during wafer sawing and polishing); (ii) guttering impurities outdiffusing from the substrate to the growth surface; (iii) smoothing the growth surface to obtain atomically-flat heterointerfaces; and (iv) reducing the crystallographic defect density (oval defects, dislocations, etc.) in subsequent epitaxial layers. The optimal buffer layer structure depends strongly on the purpose of the buffer layer and the intended device application.

In this thesis, we used a three-step ZnTe buffer layer for the growth of a high-quality GaSb layer. Since ZnTe ($L_c = 6.104\text{\AA}$) has a very close lattice constant to GaSb ($L_c = 6.094\text{\AA}$), it is regarded as one of the best buffer layers for GaSb growth in Table (3.1). And, by the combination of low- and high-temperature buffer growth, and by annealing it, we expected the successful accommodation of a large lattice mismatch (7.8%) between GaSb epitaxial layer and GaAs substrate, and a smooth surface for high-quality GaSb growth.

Zinc Telluride (ZnTe) has the molecular weight of 192.98, average atomic weight of 96.49, average atomic number of 41, and the heat of formation of -125.6 kJ/mol.^[95] The ZnTe allotrope with sphalerite structure has a lattice parameter at room temperature of 0.61020 ± 0.00006 nm.^[96] The wurtzite ZnTe allotrope lattice parameters of $a = 0.427$ nm and $c = 0.699$ nm.^[97] The X-ray density of ZnTe at 300K is 5.642g/cm³. The coefficient of thermal expansion magnitudes^[98] are 2.94×10^{-6} 1/K and 8.19×10^{-6} 1/K at 75 and 283K, respectively. The temperature dependence of the thermal expansivity between 20 and 340K can be seen in Fig. 3.1^[99].

Table 3.1 Typical properties of GaSb, ZnTe and GaAs which used in this study.

Properties	GaSb	ZnTe	GaAs
Crystal structure	ZB	ZB	ZB
Bandgap (eV) at 300K	0.7	2.26	1.43
Lattice constant (Å)	6.094	6.101	5.653
Thermal expansion coefficient (K ⁻¹)	6.7x10 ⁻⁶	8.0x10 ⁻⁶	6.0x10 ⁻⁶
Melting point (°C)	712	1295	1238
Electron mobility at 300K (cm ² /V·s)	7700	340	8500

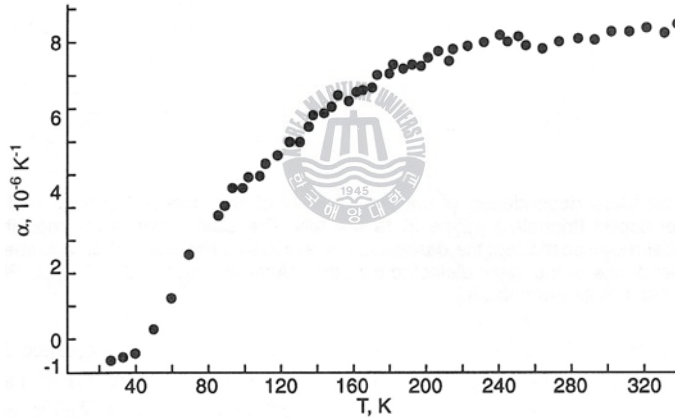


Fig. 3.1 Experimental values of ZnTe coefficient of linear thermal expansion.^[99]

The ZnTe melting point is 1568K.^[100] The magnitude of the specific heat at room temperature is 0.264J/g.K^[101] and the debye temperature of ZnTe at 293K is 204.5K^[101]. The ZnTe microhardness (square pyramid, 20-g load) is 900 ± 50 MPa^[102]. The second-order elastic constants at room temperature are $c_{11} = 71.3$ GPa, $c_{12} = 40.7$ GPa, and $c_{44} = 31.2$ Gpa.^[103]

Like the other IIb-VIb compounds, ZnTe is a direct semiconductor. The energy gap from the electrical measurements on the ZnTe:In samples is 2.12eV^[104].

The optical energy gap is 2.26 eV^[105], 2.37eV^[106], 2.381eV^[107] and 2.3941eV^[108] at 300, 77, 4 and 1.6K, respectively. The carrier effective mass in ZnTe, calculated^[109] ($m_n^* = 0.17 m_0$, $m_p^* = 1.0 m_0$) is reasonable agreement with the experimental data ($m_n^* = 0.2 m_0$ ^[110] and $m_p^* = 0.6 m_0$ ^[111]).

The electrical transport properties of ZnTe strongly depend on the method of synthesis and crustal growth, material chemical purity and defect content.^[112] The undoped ZnTe crystal usually has the p-type conductivity which varies at room temperature between 10^{-12} and 10^0 S/cm^[113].

The room temperature electron mobility reported by Fisher et al.^[114] is 340 cm²/V·s. The room temperature Hall mobility of holes is close from 100 cm²/V·s to 120 cm²/V·s.^[115]

3.1.2 Elemental Tellurium (Te) dopant source

Tellurium is a non-hydrogenic, shallow donor in III-V semiconductors. Te has both high electrical activity and a high vapour pressure and its incorporation depends strongly on growth condition especially the growth temperature.

Tellurium has not been evaporated from effusion cells containing elemental Te. Elemental Te is avoided in the ultra-high vacuum environment of the MBE system due to its high vapour pressure. Instead, Te is evaporated from compounds that have a lower vapor pressure such as SnTe, PbTe and Sb₂Te₃. Tellurium doping was done predominantly in Sb containing III-V compounds such as GaSb and GaAs_{1-x}Sb_x due to the strong amphoteric nature of Si in these compounds.

The high vapour pressure of Te makes the incorporation of Te strongly dependent on the growth conditions. A strong temperature dependence of the Te incorporation was observed in GaSb by Chiu. However, the author found that Te

incorporation is insensitive to the growth temperature for $T < 540$ °C. Efficient incorporation of Te occurred for temperature < 540 °C.

3.2 Molecular Beam Epitaxial growth techniques

Molecular beam epitaxy (MBE) has become a well-established technique for the growth of ultra-thin films and devices with precise control of thickness, doping concentration and composition. The importance of epitaxy in semiconductor devices fabrications is a direct consequence of two critical needs; for thin, defect-free single-crystal films with precisely defined geometrical, electrical, and optical properties, and for the heterojunction structures free of the interfacial impurities and defects. MBE achieves epitaxial growth by the reaction of one or more thermal atomic (or molecular beams) of constituent element with a crystalline substrate surface held at a suitable elevated temperature under-high vacuum, Essentially confined to research and development up to date, MBE has now emerged as a reliable growth technique for the realization of stringent device requirements. The uniqueness of the technique lies mainly in the tremendous precision in the controlling layer doping, thickness, and composition; in growing modulated structures whose periods are typically less than the electron mean free path; and in achieving nearing perfect heterointerfaces and surface morphologies.

3.2.1 Overview of the MBE growth chamber

Fig. 3.2 shows a schematic layout of a typical MBE growth chamber. Molecular beam of Ga, As, Sb, Se, Zn and Te are supplied from effusion cells (K-cell). The most important advantage of MBE growth is that desired profiles of mole fraction of host materials and dopants are easily obtained. In other word, each beam can be quickly switched by controlling a shutter located at the top of the each cell. This is a crucial advantage for the fabrication of GaSb:Te epitaxial layers with ZnTe buffer layer. Varying temperatures of the effusion cells can precisely control

growth velocities, molecular beam flux, and doping concentrations of each layer. Heaters of each cell are surrounded by liquid nitrogen (LN₂) shroud to prevent thermal interference between the effusion cells.

A substrate for the III-V epitaxial film growth is a GaAs (001) wafer, which is mounted on a Molybdenum (Mo) holder and placed in front of effusion cells with a movable probe arm. Substrates can be heated up to 800 °C by heaters attached at the back of the Mo holder.

Although there are some differences, the general kinetic model for epitaxial growth can be applied effectively towards understanding some of the basic physical principles behind MBE crystal growth. In this model, a reactant gas makes its way to the surface where it is first adsorbed into a highly mobile, weakly bound precursor state. The adsorbed molecule diffuses rapidly over the wafer surface until it reaches a favorable bonding site where it is incorporated into the crystal. In most cases this is a kink site created by the discontinuity between the previous complete monolayer and the partial monolayer in the process of being formed Fig. 3.3.

A source molecule reaches the surface and is chemisorbed into a weakly bound, highly precursor state. The adsorbed molecule rapidly makes its ways around the wafer surface until it reaches the favorable bonding site, where it is then incorporated into the crystal.

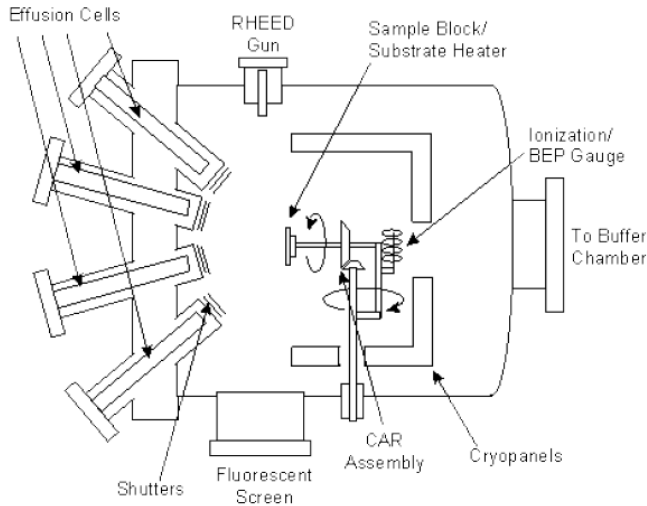


Fig. 3.2 Schematic layout of a typical MBE growth chamber

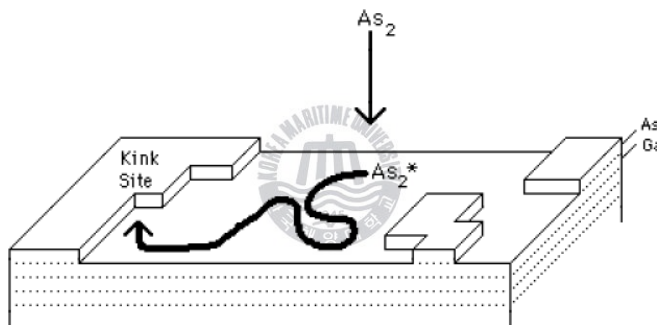


Fig. 3.3 Schematic illustration of simple epitaxial growth mechanism

3.2.2 Reflection High Energy Electron Diffraction (RHEED)

Another merit of MBE growth is that the condition of the epitaxial films can be monitored during growth. The chamber includes a Reflection High Energy Electron Diffraction (RHEED), a technique in which a beam of electrons is bounced off the wafer surface onto a fluorescent screen producing a pattern that is indicative of the quality of the crystal being grown, system for observation of the surface atomic-lattice condition.

Both the electron gun and fluorescent screen are protected from the growth fluxes by cryopanelling. Additional baffling is provided in MBE applications

employing electron beam evaporators to preclude stray electrons from causing an unacceptably high background glow on the screen.

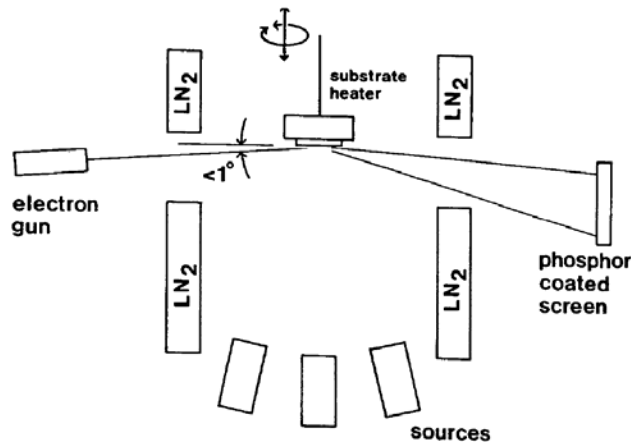


Fig. 3.4 Schematic illustration of typical RHEED geometry.

A spotted RHEED pattern indicates the presence of a rough surface and is generally considered undesirable after the initial stages of material growth. When good material is being grown properly, the RHEED pattern contains two features. Streaks, or main lines as they are sometimes called, indicate the presence of a reasonably smooth crystalline surface. Reconstruction lines on the other hand are brought about by the crystal growth processes taking place on the surface. The presence of streaks and reconstruction lines in the RHEED pattern during MBE growth usually indicates that good crystalline material is being deposited.

To maintain a high vacuum condition at all times, a turbo molecular pump is used as well as a gate valve separates the growth chamber and transfer chamber. Background pressure in the growth chamber is about 10^{-10} Torr.

3.2.3 MBE growth procedures

The GaAs (001) wafers are used as substrate for the epitaxial films. Before loading into the chamber, the GaAs wafers were prepared as the following processes:

- (1) The substrates are cut with the Diamond cutter from the back side of the substrate in $1\text{cm} \times 0.5\text{cm}$ size.
- (2) The substrates are rinsed in acetone (100ml) for 15 minutes, and rinsed in methanol (150ml) for 15 minutes.
- (3) They were then rinsed thoroughly in deionized water (DI) (200ml) for 5 minutes
- (4) They were dried under a stream of dry Nitrogen.
- (5) The wafers were etched for 2 minutes in 1 NH_4OH : 2 H_2O_2 : 50 DI water.
- (6) The etch was quenched by flooding three beakers with DI water for 1 minute each.
- (7) They were dried under a stream Nitrogen, and
- (8) They were attached to the Mo block by Indium (In) solder.

The MBE growth was conducted according to the following procedures.

- (1) The shroud is cooled by supplying liquid nitrogen.
- (2) Each effusion cell is heated to the set temperature, and the molecular beam for each cell is monitored by beam flux monitor.

- (3) The loading chamber is evacuated down to 10^{-8} Torr. Then a substrate mounted on a Mo block is moved to transfer chamber. Finally, the substrate is loaded into the growth chamber.
- (4) First, the substrate is heated to around $640\text{ }^{\circ}\text{C}$ for 15 minutes to move any surface oxide of GaAs substrate (see Table3.2), then down to growth temperature $450\text{ }^{\circ}\text{C}$.
- (5) Epitaxial growth is starting by opening cell shutters (for, Zn, Te, Ga, Sb, etc.)

After MBE growth, the substrate is cooled to less than $150\text{ }^{\circ}\text{C}$ and moved back to the loading chamber.

Table 3.2 Thermal etching condition of GaAs substrate.

Degree of vacuum	$\sim 10^{-10}$ Torr
Annealing temperature	$640\text{ }^{\circ}\text{C}$
Annealing time	15 mins

3.2.4 Fabrication of the high quality n-type GaSb:Te epitaxial layers

One set of Te-doped GaSb layers was grown on (001) GaAs substrates by MBE. GaAs substrates were degreased by organic solvents of ethanol and acetone and etched with a solution of $\text{NH}_4\text{OH}:\text{H}_2\text{O}_2:\text{H}_2\text{O}$. The substrates were thermally deoxidized at $580\text{ }^{\circ}\text{C}$ for 10 min in a chamber as described procedure in Section 3.2.

In Type I, the GaSb:Te layer was directly grown at $480\text{ }^{\circ}\text{C}$ on the GaAs substrate. The growth rate of the GaSb:Te layer was 15 nm/min , and the finally obtained film thickness was 1400 nm .

On the contrary, in Type II, a ZnTe buffer is inserted between the GaSb:Te layer and the GaAs substrate. First, the ZnTe buffer was slowly grown on the GaAs substrate at 300°C at a rate of 1 nm/min. (Its film thickness was 300 nm.) Subsequently, the GaSb:Te layer were grown under the same condition of Type I. On the other hand, Te-cell temperature was maintained at 220 °C for n-type doping for both samples.

3.3 Hall Effect measurement

3.3.1 Experimental setup of Hall measurement

Electrical characterization can give considerable information about the disorder in terms of purity of epitaxial layers. Such information is important for the evaluation and control of growth parameters used to prepare high quality epitaxial layers for device applications. Electrical characterizations such as mobility, resistivity and carrier concentration are obtained by performing Hall Effect measurements.

The Hall measurement set up used in this study is shown in Fig. 3.5 schematically. It is consisted of a sample holder including probe stage, a power control unit, a magnetic system, and a low-temperature cryostat. As the magnetic system is consist of a magnet, a power supply and a Gauss-meter. The temperature control was carried out by the combination low-temperature cryostat and He gas was used to lower temperature until 10K.

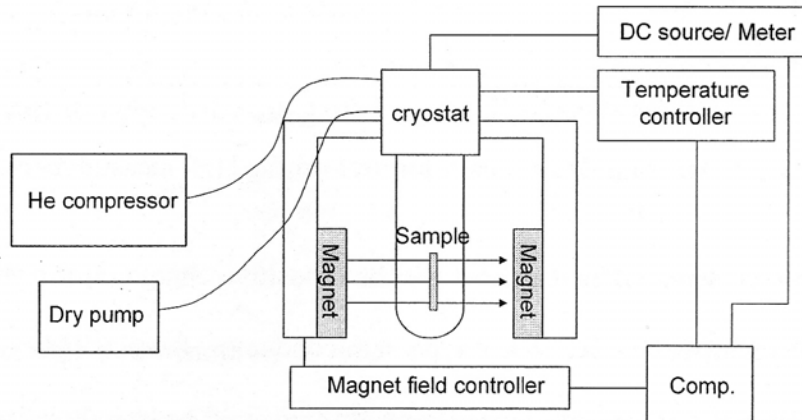


Fig. 3.5 Schematic illustration of Hall Effects measurement equipment.

3.3.2 Hall Effects

The Hall Effect is a consequence of the forces that are exerted on moving charges by electric and magnetic fields. The Hall Effect is used to distinguish whether a semiconductor is n-type or p-type and to measure the majority carrier concentration and mobility.^[116]

Fig.3.6 shows a sample in the form of a rectangular bar oriented with its longest axis along the x axis. The electric field F is applied along the x axis while the magnetic field B is still along the z axis. According to Lorentz's law, when electrons start to drift along the x axis under the influence of the electric field, they also experience a force in the y-direction. This results in a current in the y-direction although there is no applied electric field in that direction.

In a p-type semiconductor, there will be a positive charge on the $y=0$ surface of the semiconductor, while, in a n-type semiconductor, there will be a negative charge on the $y=0$ surface. The magnetic field force will be exactly balance by the induced electric field force. This balance may be written as following formula.

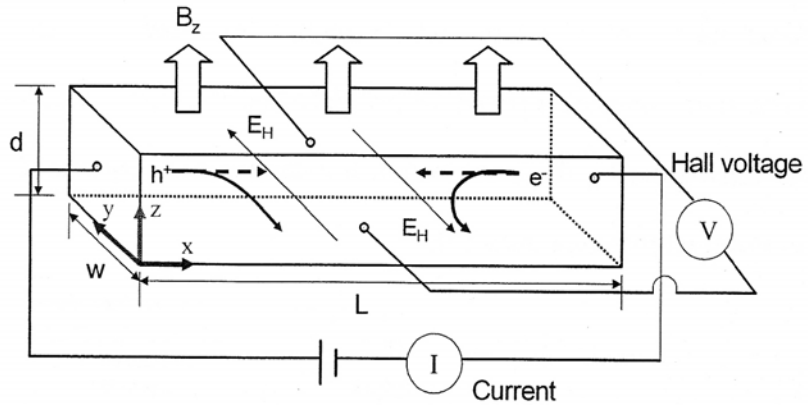


Fig. 3.6 The sample geometry for performing Hall measurement.

$$F = q [E + v \times B] = 0 \quad (3.1)$$

The induced electric field in the y -direction is called the hall field. The hall field produces a voltage across the semiconductor which is called the hall voltage. We can write such like that.

$$V_H = +E_H W \quad (3.2)$$

E_H is assumed positive in the $+y$ direction and V_H is positive with the polarity shown. In a p -type semiconductor, holes are the majority carrier. While, in a n -type semiconductor, electrons are the majority carrier, The polarity of the Hall voltage is used to determine whether an extrinsic semiconductor is n -type or p -type semiconductor respectively.

$$n = -\frac{I_x B_z}{edV_H} \quad (3.3)$$

$$p = \frac{I_x B_z}{edV_H} \quad (3.4)$$

We can also obtain the low-field electron, hole mobility respectively.

$$m_n = \frac{I_x L}{enV_x W d} \quad (3.5)$$

$$m_p = \frac{I_x L}{epV_x W d} \quad (3.6)$$

3.3.3 Van der Pauw method

Samples are often grown in the form of thin epitaxial films on some insulation substrates. The extension of the Hall technique to such thin film was developed by Van der Pauw.^[117] Fig 3.7 shows the Van der Pauw method of measuring the Hall coefficient and resistivity in a thin sample. The current is fed through the contacts 3 and 4 while the Hall voltage is measured across the contacts 1 and 2. The sample shape in Fig. 3.7 has the advantage of keeping the current from the Hall voltage contacts.

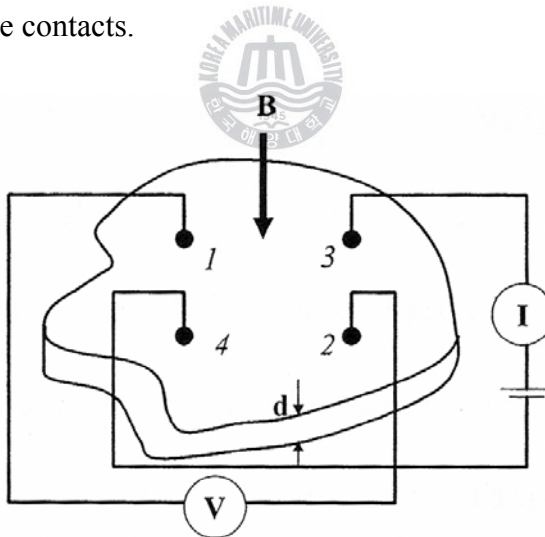


Fig. 3.7 Schematic diagram of Van der Pauw method.

To minimize the error in the measurement of the Hall voltage due to the fact that the current flow may not be perpendicular to the line joining the contacts 1 and 2, one usually measures the voltage both with the magnetic field $V_{12}(\pm B)$ and without the field $V_{12}(0)$. Van der Pauw shows that the Hall coefficient is given by

$$R_h = \frac{[V_{12}(B) - V_{12}(0)]d}{I_{34}B} = \frac{[V_{12}(B) - V_{12}(-B)]d}{2I_{34}B} \quad (3.7)$$

d is the thickness of the film, B is the magnetic field and I_{34} is the current flowing from contact 3 to 4. The sample resistivity ρ can also be measured with the Van der pauw method. In this case two adjacent contacts such as 2 and 3 (I_{23}) are used as current contracts while the two remaining contacts are used for measuring voltage (V_{41}). The resultant resistance is defined as $R_{41,23}$.

$$R_{41,23} = |V_{41}| / I_{23} \quad (3.8)$$

Another measurement is that current is sent through the contacts 1 and 3, then the voltage is measured across the contact 2 and 4. From the resulting resistance $R_{24,13}$ and $R_{41,23}$, Resistivity ρ can be calculated with following expression,

$$\rho = \frac{\pi d (R_{24,13} + R_{41,23}) f}{2 \ln 2} \quad (3.9)$$

f is the factor that depends on the ration $R_{24,13} / R_{41,23}$. Usually a large value for this ratio is undesirable and suggests that the contacts are bad or the sample is inhomogeneously doped.

3.4 High-resolution X-ray Diffraction (HRXRD) measurement

3.4.1 Experimental setup of HRXRD

High-resolution X-ray diffraction (HRXRD) is a powerful tool for nondestructive ex-situ investigation of epitaxial layers, thickness, the build-in strain and strain relaxation, and the crystalline perfection related to dislocation density.

In study, HRXRD rocking curve were measured by a Hybrid 4 crystal bound monochromator as shown in Fig. 3.8. The main components of this instrument are

x-ray tube; monochromator consists of blocks made from dislocation-free germanium single crystals. The four crystal Ge(220) monochromator produces a beam with very low divergence and small wavelength spread.

To investigate structural quality of compound semiconductor, symmetric plane (004) and asymmetric plane (111) and (115) planes are measured by HRXRD. The (004) Bragg reflection is used to determine the lattice constant. Mosaicity (tilt and twist) want determined by series of X-ray measurement. From the tilt, twist angle, it is possible to determine the screw, edge dislocation densities respectively.

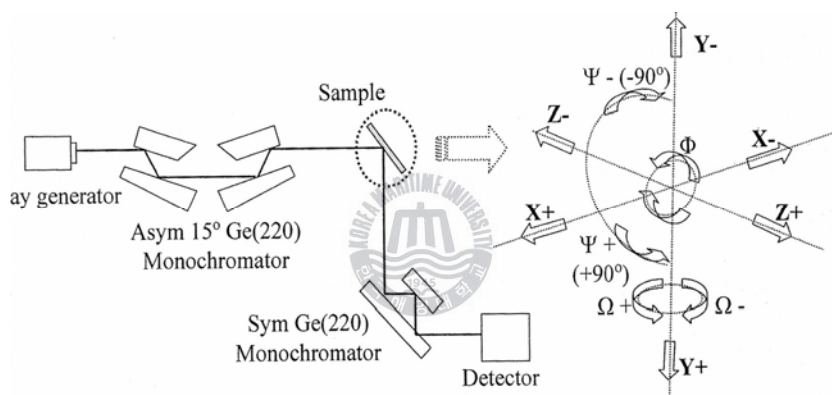


Fig. 3.8 Schematic illustration of HRXRD geometry

3.4.2 ω scan (rocking curve) and ω - 2θ scan

The simplest and most useful description of crystal diffraction is obtained by Bragg law.

$$2d \sin \theta = n\lambda \quad (3.10)$$

where n is an integer representing the order of diffraction, λ is wavelength, d is the interplanar spacing of the reflecting and θ is the angle of incidence and of diffraction of the radiation relative to the reflection plane. The requirement for the angle of incidence to equal that of diffraction is directly seen in Fig. 3.9

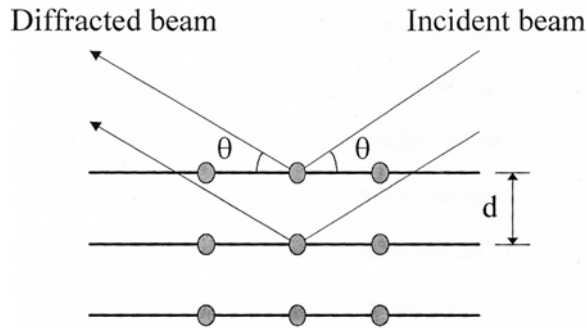


Fig. 3.9 Diffraction of a plane corresponding to Bragg law

Diffraction for a given plane and wavelength does not take place over the zero angular range defined by the Bragg law, but over a small finite range. This range, called the ‘rocking curve’, varies tremendously and it shows the structural quality sensitively.^[118] Conventional diffractometers use a ω - 2θ scan for measuring symmetric Bragg reflections. For such a scan, the detector is rotated twice as fast and in the same direction around the diffractometer axis as the sample. In reciprocal space, the motion of sample and detector corresponds to a change of wave vector k_s , which moves along the reciprocal lattice vector G_{hkl} . During the motion, the angle ω between the incident beam and the sample surface changes. In ω scan, the detector is fixed in position with wide open entrance slits and the sample is rotated. In reciprocal space, this corresponding to a path is as shown in Fig. 3.10.^[119]

When we consider about rocking curve of heteroepilayers, there exist differences of diffraction angle between the layer and the substrate, which is caused by tilt ($\delta\theta$) or mismatch (δd). Double or multiple peaks will therefore arise in the rocking curve. Peaks may be broadened by defects if these give additional rotations to the crystal lattice, and there will also be small peaks arising from interference between waves scattered from the interfaces, which will be controlled by the layer thickness. The material will show different defects in different regions. Table 3.3 summaries the influence on the rocking curve of the important parameters.^[120]

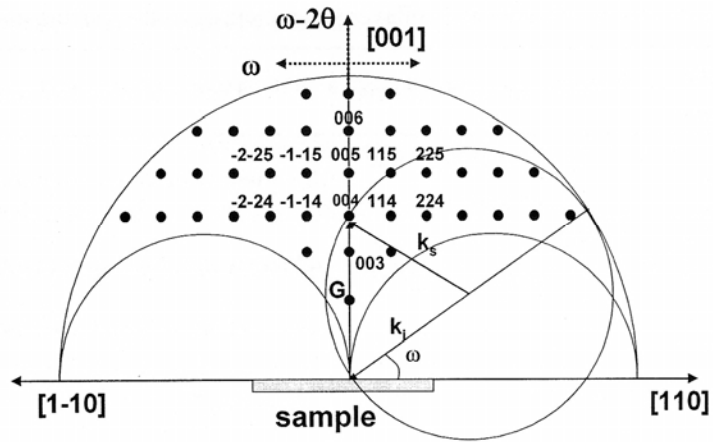


Fig. 3.10 Reciprocal space map showing accessible range for Bragg reflection measurements.



Table 3.3 The effect of substrate and epilayer parameters upon the rocking curve.

Material parameter	Effect on rocking curve	Distinguishing features
Mismatch	Splitting of layer and substrate peak	Invariant with sample rotation
Misorientation	Splitting of layer and substrate peak	Changes sign with sample rotation
Dislocation content	Broadening peak	Broadening invariant with beam size. No shift of peak with beam position on sample
Mosaic spread	Broadening peak	Broadening may increase with beam size, up to mosaic cell size.
Curvature	Broadening peak	Broadening increases linearly with beam size. Peak shifts systematically with beam position on sample.
Relaxation	Changes splitting	Different effect on symmetrical and asymmetrical reflection.
Thickness	Affecting intensity of Peak	Integrated intensity increases with layer thickness, up to a limit
Inhomogeneity	Effect vary with position on sample	Individual characteristics may be mapped

Chapter 4 Electrical transport properties of GaSb:Te epitaxial layers

4.1 Introduction

There has been renewed interest in the narrow band gap III-V compound semiconductors as GaSb for opto-electronic applications, high-frequency electronics, and magnetic field sensors. In order to characterize the electrical transport properties of these films and to produce films suitable for electron devices having current flow parallel to the epitaxial interface it is important to grow on electrically insulating substrates. Unfortunately there are no lattice matched, insulating substrates for epitaxial growth, so insulating substrates which have a large lattice mismatch with the epitaxial layer have been employed. In this study we report our growth studies of GaSb on GaAs by molecular beam epitaxy (MBE). A unique feature of our growth technique is the employment of Zn-terminated 3-steps ZnTe buffer layer at the GaAs interface grown by MBE process. It will be demonstrated that the use of the ZnTe interface layer leads to epitaxial GaSb having electrical and structural properties approaching that of good GaSb layer.

There are several methods used in the calculation of electron drift mobility, namely: variational principle (VP), iterative method (IM), Monte Carlo (MC) method, relaxation time approximation (RTA), and Matthiessen rule (MR) formalism.

In Table 4.1, we have summarized some of the common methods used to evaluate transport properties; included are the advantages and disadvantages of each method. While the methods described are the most frequently employed, other techniques such as the energy loss method and so called dynamical method are also used to calculate electron mobility.

Table 4.1 A summary of the various methods of evaluating transport properties of semiconductors.

Method	Advantages	Disadvantages	Remarks
Variational Method	The effect of optical phonon scattering can be determined without having to calculate a relaxation time.	<ol style="list-style-type: none"> 1. Difficult to implement. 2. Inclusion of some scattering mechanisms may render the BTE to be solvable analytically. 3. Difficult to evaluate the effect of individual scattering mechanisms. 	The most exact method for solving the BTE.
Iterative method	The effect of optical phonon scattering can be determined without having to calculate a relaxation time.	<ol style="list-style-type: none"> 1. Requires extensive computing time. 2. Difficult to evaluate the effect of individual scattering mechanisms. 	This is found to be not satisfactory for moderately doped samples of GaAs. Also requires the independences of individual scattering mechanisms, as in RTA and MR.
Monte Carlo method	<ol style="list-style-type: none"> 1. Accurate for determining the mobility under extreme conditions, such as huge fields and low dimensions. 2. Nonparabolicity of bands or realistic band structure can be easily studied. 3. Fluctuation phenomena can be easily studied. 	<ol style="list-style-type: none"> 1. Suffers from large uncertainty at low field. 2. Requires large resources in computer memory and computing time. 	Observed to be in good agreement with Matthiessen's rule for InGaAs alloys.
Relaxation time approximation or Matthiessen's rule	<ol style="list-style-type: none"> 1. Easy to implement. 2. Permits evaluation of the effect of individual scattering mechanisms (MR only). 	<ol style="list-style-type: none"> 1. Requires an estimate of the relaxation time for optical phonon scattering, which may be inaccurate over a particular temperature range. 2. An approximate solution to the BTE is obtained. 	The most widely used of the above methods (as observed in the literature), providing good agreement with experimental data.

In this work, we consider only the effect of carrier density and compensation ratio (N_A/N_D) on the theoretical electron mobility in GaSb. We choose MR to calculate electron drift mobility in GaSb epitaxial layers, since it is arguably the most convenient to implement and the relative strength of the individual scattering mechanisms can be easily evaluated and visualized. *A fortifier*: this method is found to give good agreement with the experimental results of III-V binary semiconductors and their ternary alloys. Good agreement with experimental results is often obtained by treating the compensation ratio as the only adjustable parameter since carrier concentration is normally known from experiments.

4.2 Structural properties of GaSb:Te epitaxial layers

High-resolution X-ray diffraction (HRXRD) measurements results are shown as Table 4.2.

Table 4.2 HRXRD measurements result of GaSb:Te epitaxial layers [GaSb:Te/GaAs (Type I) and GaSb:Te/ZnTe/GaAs (Type II)]

XRD FWHM	Type I	Type II
ω (004)	972arcsec	516 arcsec
ω (111)	957 arcsec	632 arcsec
ω (115)	1004 arcsec	954arcsec
$\omega - 2\Theta$ (004)	205 arcsec	155 arcsec
$\omega - 2\Theta$ (111)	81 arcsec	59 arcsec
$\omega - 2\Theta$ (115)	377 arcsec	248 arcsec

(a)

Residual strain(%)	Type I	Type II
(004)	-0.172	-0.115
(111)	0.047	0.021
(115)	0.120	0.040

(b)

Fig. 4.1 shows the Williamson-Hall plot of the two samples, which can be calculated the dislocation density of the samples obtained from ω scans for (004), (111), and (115) planes. Types I and II have dislocation densities $2.5 \times 10^7 \text{ cm}^{-2}$ and $4.4 \times 10^6 \text{ cm}^{-2}$, respectively. The inset of Fig.4.1 shows ω scan curves for (004) plane in types I and II, measured by High-Resolution X-Ray Diffractometer (HRXRD). Type II (GaSb:Te/ZnTe/GaAs) has 2 times narrower linewidth and 5 times large intensity than type I (GaSb/GaAs).

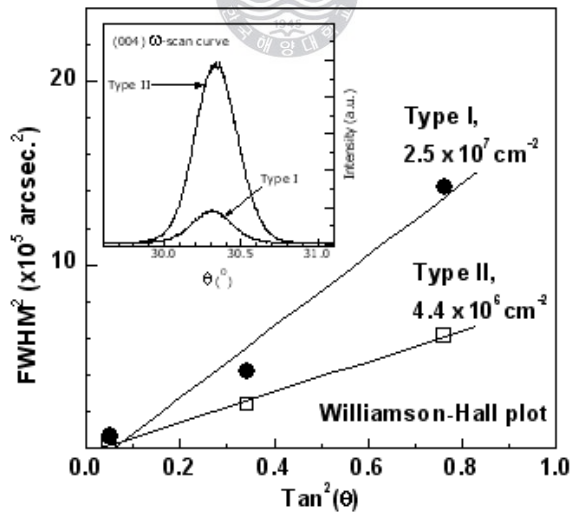


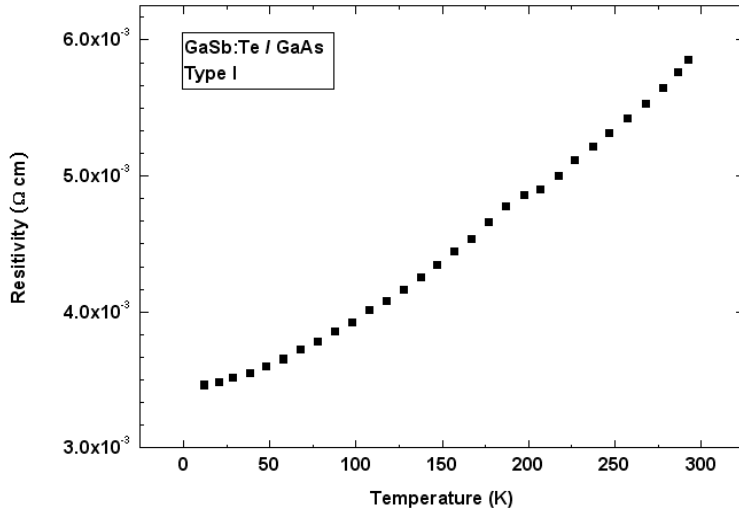
Fig. 4.1 Williamson-Hall plot for symmetric and asymmetric reflection for using dislocation density of GaSb:Te epitaxial layers.

4.3 Electrical properties of GaSb:Te epitaxial layers

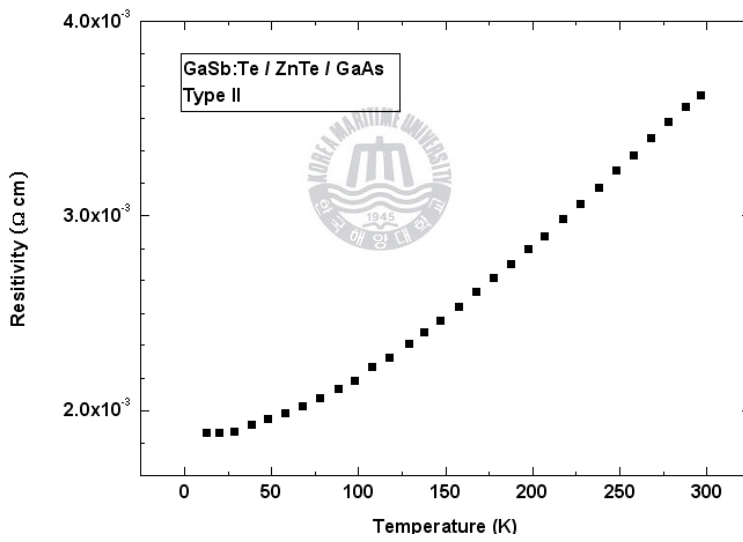
Four-contacts of Au–Ge alloy (using 0.25g of Au-Ge alloy balls) was evaporated and formed 1.8 μm thickness on the GaSb:Te doping epitaxial layers. Hall Effect measurements were performed at the temperature range between $10 \leq T \leq 300\text{K}$, the 3500 Gauss magnetic field, maintained current 0.1A for both samples. The Hall mobility showed that Type II has 2.5times higher than Type I at room temperature and at 2.7 times higher than at 10K. As well as, Type II has 1.6 times lower resistivity than Type I at room temperature and 1.8 times lower resistivity at 10K measurements. It clearly shows that ZnTe buffer improves carrier mobility in Type II sample.

The measurement results are as shown in Table 4.2, Fig. 4.2, 4.3 and 4.4.



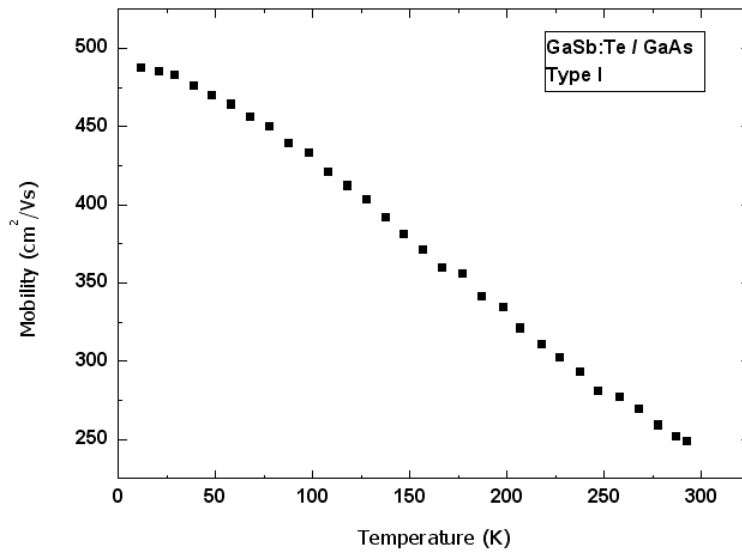


(a)

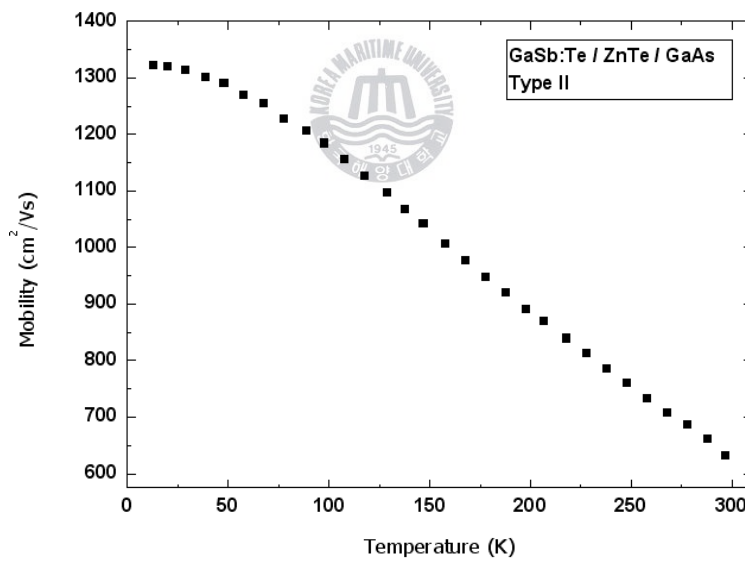


(b)

Fig. 4.2 Temperature dependent resistivity measurement of GaSb:Te epitaxial layers

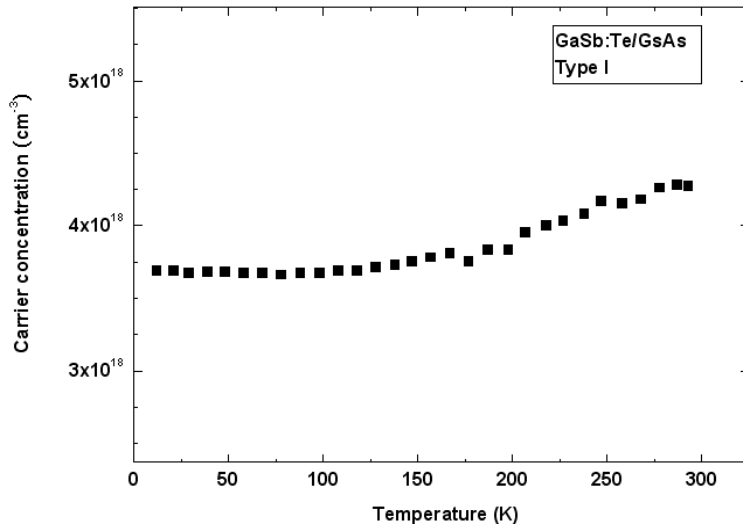


(a)

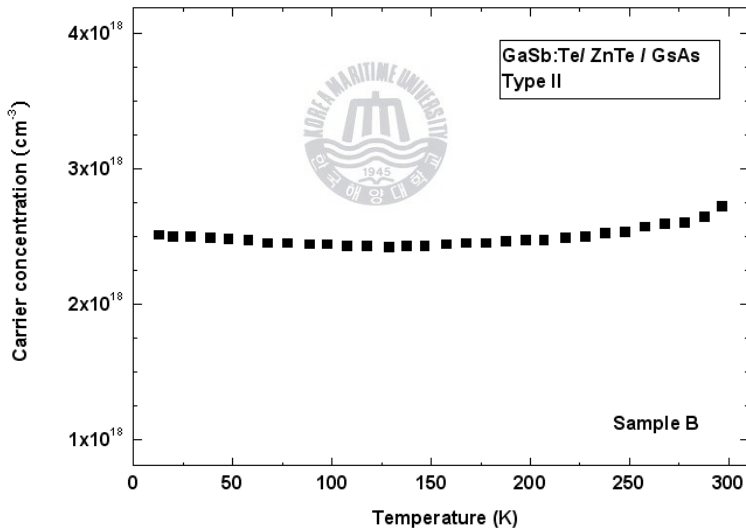


(b)

Fig. 4.3 Temperature dependent mobility measurement of GaSb:Te epitaxial layers



(a)



(b)

Fig. 4.4 Temperature dependent carrier concentration measurement of GaSb:Te epitaxial layers

Table 4.3 Temperature dependent Hall Effect measurements of GaSb:Te epitaxial layers

	Temperature	Resistivity($\Omega\cdot\text{cm}$)	Mobility(cm^2/Vs)	Carrier Concentration(cm^{-3})
Type I	RT	5.85×10^{-3}	249	4.27×10^{18}
	10K	3.46×10^{-3}	487	3.69×10^{18}
Type II	RT	3.62×10^{-3}	631	2.72×10^{18}
	10K	1.88×10^{-3}	1321	2.51×10^{18}

4.4 Correction by two-layer Hall Effect model

To explain the role of ZnTe buffer on the electrical properties of GaSb:Te layers. We analysis using the to the Brooks-Herring scattering theory, based on the two-layer Hall effect model, with considering the four major scattering mechanisms such as polar phonon, deformation potential, ionized impurity and dislocation scattering. The two-layer model is a quantitive way to elucidate both the bulk and interfacial electrical properties by considering the two-layers for the charge transport. Considering the layer 1 (bulk layer) and 2 (interface layer), the measured quantities, μ_H and n_H can be expressed, based on multiband (or multi layer) analysis, as^[121]:

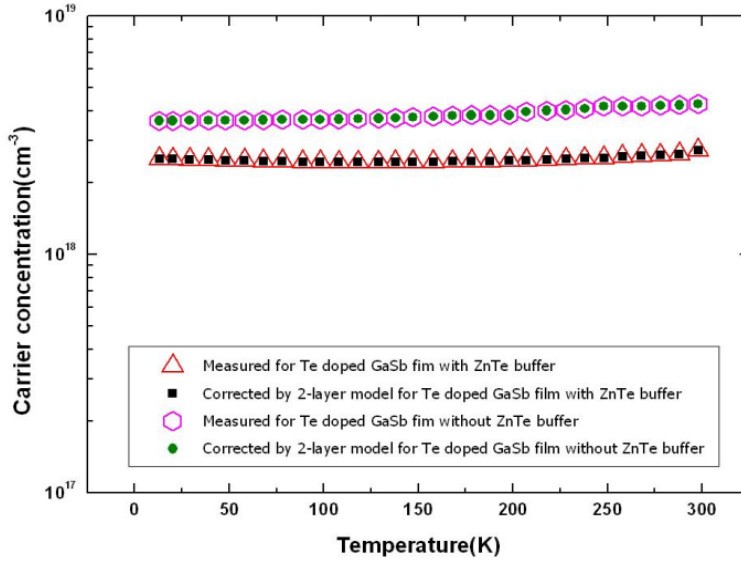
$$\mu_H = (\mu_{H1}^2 n_{H1} + \mu_{H2}^2 n_{H2}) / (\mu_{H1} n_{H1} + \mu_{H2} n_{H2}) \quad (4.1)$$

$$n_H = (\mu_{H1} n_{H1} + \mu_{H2} n_{H2})^2 / (\mu_{H1}^2 n_{H1} + \mu_{H2}^2 n_{H2}) \quad (4.2)$$

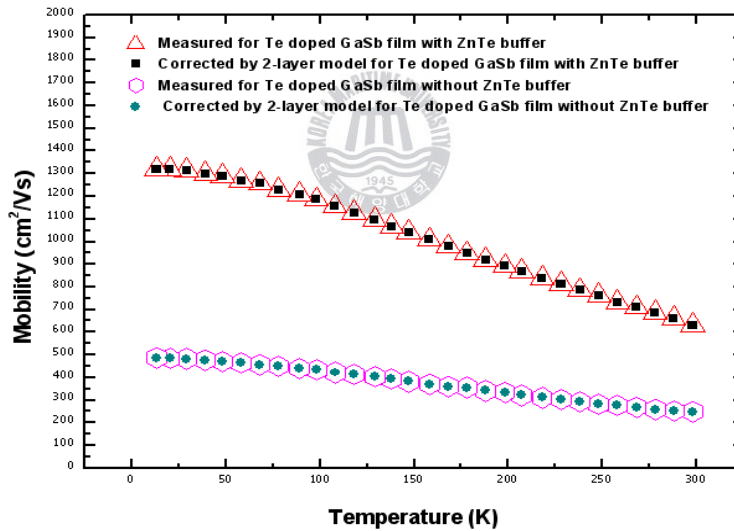
At very low temperature, the interfacial layer must be dominant so that $\mu_H = \mu_{H2} = \mu_2$ and $n_H = n_{H2} = n_2$. Here, μ_2 and n_2 indicated the values at the lowest measured temperature. In order to correct the measured values by considering the effect of interface layer (in other words, to extract the bulk layer property from the measured bulk+ interface layer property), μ_2 and n_2 should be taken, if possible, from the lowest temperature, where the effect of the interface layer is dominant.

Fig 4.5 (a) and (b) show measured and corrected carrier concentration and mobility curves, respectively from the GaSb:Te epitaxial layers.





(a)



(b)

Fig. 4.5 Temperature dependent measured and corrected (a) Hall concentration and (b) Hall mobility curves for the GaSb:Te epitaxial layers.

4.5 Fitting of temperature dependent carrier concentration curves

Charge balanced equation is used to fit the temperature dependent carrier concentration curves.^[122]

$$n + N_A + N_{dis} / c = \frac{N_D}{1 + n / \phi} \quad (4.3)$$

where $\phi = [(g_0 / g_1) N_c' \exp(\alpha / k_B)] T^{3/2} \exp(-E_D / kT)$. Here g_0 and g_1 are the degeneracies of the unoccupied and occupied states ($g_0=1$ and $g_1=2$), respectively, N_c' is the effective conduction band density of states at $T=1K$, E_{D0} is the activation energy of the donor at $T=0$, and α is the temperature coefficient defined by . The quantity N_{dis} is the areal concentration(m^{-2}) of the threading edge dislocations, and N_{dis}/c is the volume (m^{-3}) concentration of the associated acceptors. The measured electron concentration curves were fitted by using the Eq (4.3). Here, the fitting parameters were N_A , N_D , E_D , N_{dis} and Φ . (Acceptor concentration, donor concentration, donor level, dislocation density) The n values are determined by the fitting of the measured data by using the Eq (4.3). If the fitting is successful, the determined n values should be the same to the values of n_H determined by the correcting procedures with the Eq (4.2).

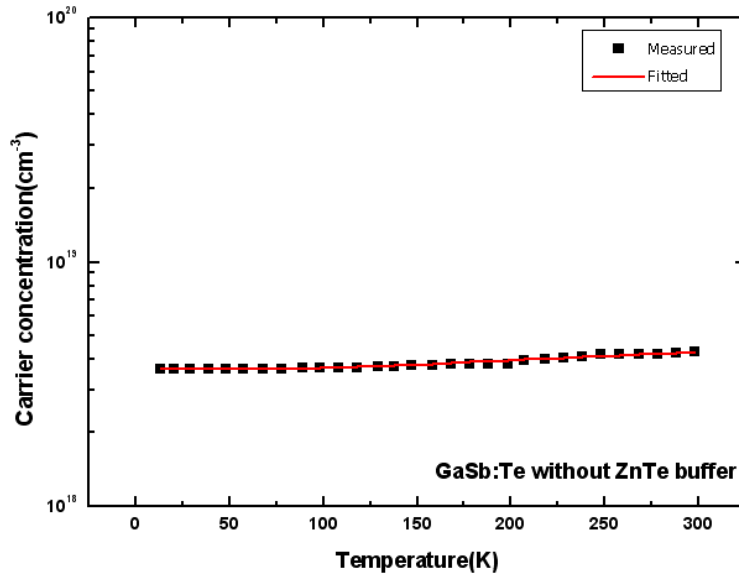
$$n_{two-band} = \frac{(n\mu_d + n_{ib}\mu_{ib})^2}{n\mu_d\mu_H + n_{ib}\mu_{ib}^2} \quad (4.4)$$

$$\mu_{two-band} = \frac{n\mu_d\mu_H + n_{ib}\mu_{ib}^2}{n\mu_d + n_{ib}\mu_{ib}} \quad (4.5)$$

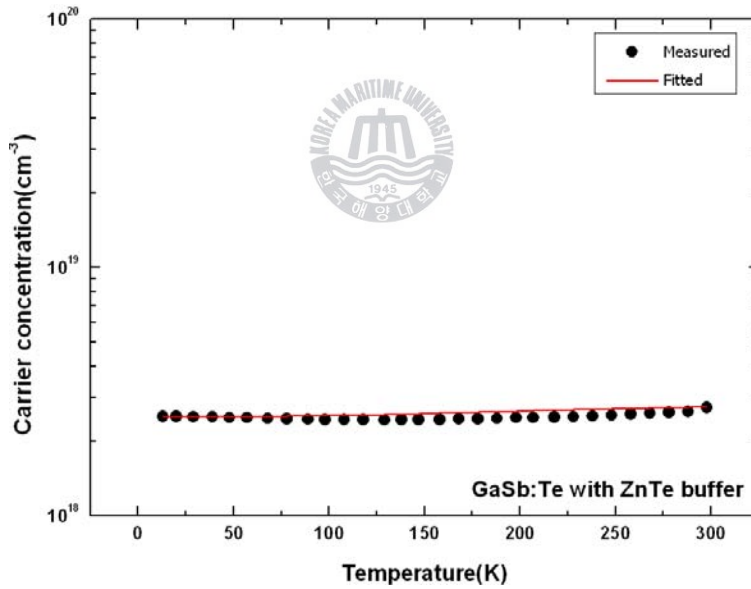
where μ_H and μ_d are the conduction-band (cb) hall and drift mobilities, respectively, ($\mu_d = \mu_H$, assuming a Hall factor of r of unity), μ_{ib} the impurity-band (ib) mobility, n is the cb electron concentration and $n_{ib} = N_A$.

No distinction is made between hall and drift mobilities for the impurity band, since we are only roughly modeling this region anyway, and it is further assumed that these mobilities are temperature independent.

Fig. 4.6 shows the measured and fitting carrier concentration curves for the (a) GaSb:Te/GaAs (Type I) and (b) GaSb:Te/ZnTe/GaAs (Type II) respectively.



(a)



(b)

Fig. 4.6 The measured and fitting carrier concentration curves for the (a) GaSb:Te/GaAs (Type I) and (b) GaSb:Te/ZnTe/GaAs (Type II)

4.6 Calculation of mobility curves by the Boltzman transport equations

The mobility curves can be theoretically predicted by considering various scattering mechanisms. In order to obtain theoretical mobility curves, four scattering mechanisms: 1) polar phonon scattering, 2) deformation potential scattering, 3) ionized impurity scattering (degenerated) and 4) dislocation scattering (degenerated) were considered in this study. Boltzman transport equation (BTE)^[123,124] solved by Rode's iterative method^[125] were used in this study to calculate the mobilities.

4.6.1 Ionized impurity scattering

Impurities are foreign atoms in the solid, which are efficient scattering centers especially when they have a net charge. Ionized donors and acceptors in a semiconductor are a common example of such impurities. The amount of scattering due to electrostatic forces between the carrier and the ionized impurity depends on the interaction time and the number of impurities. Larger impurity concentrations result in a lower mobility. The dependence on the interaction time helps to explain the temperature dependence. The interaction time is directly linked to the relative velocity of the carrier and the impurity, which is related to the thermal velocity of the carriers. The thermal velocity increases with the ambient temperature so that the interaction time decreases. Thereby, the amount of scattering decreases, resulting in a mobility increase with temperature. To first order, the mobility due to impurity scattering is proportional to $T^{3/2}/N_I$, where N_I is the density of charged impurities.

Ionized impurities scatter electrons through their screened coulomb potential:

$$\Delta V = \frac{Ze^2}{4\pi \epsilon r} e^{-r/\lambda_D} \quad (4.6)$$

where Ze is the ionic charge, and λ_D is the Debye length: in the non-degenerate case, $\lambda_D^2 = \epsilon kT / e^2 n$ for free-electron screening alone, or $\lambda_D^2 = \epsilon kT / e^2 \{n + (n + N_A)[1 - (n + N_A) / N_D]\}$ if the donors are not completely ionized.

The mobility associated with B-H ionized-impurity scattering is

$$\begin{aligned} \mu_{ii} &= \frac{e \langle \tau_{ii}(E) \rangle}{m^*} = \frac{e}{m^*} a_{ii} \frac{\int_0^\infty \tau_{ii}(E) E^{3/2} \frac{\partial f_0}{\partial E} dE}{\int_0^\infty (E) E^{3/2} \frac{\partial f_0}{\partial E} dE} \\ &= \frac{e}{m^*} a_{ii} \frac{\int_0^\infty E^3 [\ln(1+y') - y' / (1+y')]^{-1} \frac{\partial f}{\partial E} dE}{\int_0^\infty E^{3/2} \frac{\partial f_0}{\partial E} dE} \end{aligned} \quad (4.7)$$

We first consider non-degenerate statistics. Then $\partial f_0 / \partial E \propto \exp(-E / kT)$ so that

$$\mu_{ii} = \frac{128 \sqrt{2\pi^{1/2}} \epsilon^2 (kT)^{3/2}}{N_I Z^2 e^3 m^{*1/2} [\ln(1+y) - y / (1+y)]} \quad (4.8)$$

where $y = 24 \epsilon m^* (kT)^2 / \hbar^2 e^2 n$. This value of y is obtained by realizing that the bracketed term in the integral varies slowly with E , and thus can be replaced by its values at the integrand maximum, i.e. at $E \approx 3kT$. Note that μ_{ii} in Eq. (4.8) carries with temperature as $T^{3/2}$, and thus ionized-impurity scattering almost always dominates at a low enough temperature in any semiconductor.

For degenerate statistics, $\partial f_0 / \partial E \approx \delta(E - E_F)$ in Eq. (4.7), and thus $\mu_{ii} = e \tau_{ii}(E_F) / m^*$. For this case,

$$k^2 \simeq k_F^2 \simeq 2m^* E_F / \hbar^2 \simeq (3\pi^2 n)^{2/3} \quad (4.9)$$

and the generalized form of λ_D^2 then becomes

$$\lambda_D^2 = \frac{\epsilon kT \mathfrak{I}_{1/2}(\eta)}{e^2 n \mathfrak{I}_{-1/2}(\eta)} \rightarrow \frac{\epsilon kT \eta_F^{3/2} \Gamma(3/2)}{e^2 n \eta_F^{1/2} \Gamma(5/2)} = \frac{\epsilon kT}{e^2 n} \frac{2 E_F}{3 kT} = \frac{2 \epsilon E_F}{3 e^2 n} \quad (4.10)$$

where $\eta_F \equiv E_F / kT \gg 1$. Thus, μ_{ii} becomes

$$\mu_{ii} = \frac{24\pi^3 \epsilon^2 \hbar^3 n}{N_i Z^2 e^3 m^{*2} [\ln(1 + y_F) - y_F / (1 + y_F)]} \quad (4.11)$$

where $y_F = 3^{1/3} 4\pi^{8/3} \epsilon \hbar^2 n^{1/3} / e^2 m^*$. Note that μ_{ii} for the degenerate case is more strongly dependent on m^* than that for the nondegenerate case, and also has no explicit on T .



4.6.2 Dislocation Scattering

Charged dislocations act as acceptor traps and this is the source of dislocation scattering. the mobility by charged dislocation scattering (degenerated) scattering is given by^[124],

$$\mu_{dis,deg} = \frac{4 \times 3^{2/3} e c^2 n^{2/3}}{\pi^{8/3} \hbar N_{dis}} [1 + y]^{3/2} \quad (4.12)$$

where $y = (2 \times 3^{1/3} \pi^{8/3} \hbar^2 \epsilon n^{1/3}) / (e^2 m^*)$

4.6.3 Acoustic phonon: deformation potential

The acoustic-mode lattice vibrations induce changes in lattice spacing, which change the band gap from point to point. Since the crystal is ‘deformed’ at these

points, the potential is called the deformation potential. The corresponding relaxation time can be written

$$\tau_{dp} = \frac{\pi \hbar^4 \rho s^2}{\sqrt{2} E_1^2 m^{*3/2} (kT)} E^{-1/2} \quad (4.13)$$

where ρ is the crystal density, s is the properly averaged velocity of sound, and E_1 is the deformation potential. Here $\rho s^2 = c_l$, the longitudinal elastic constant about $(1.044 \times 10^{11} \text{N/m}^2)$ in GaSb. Also the best value of $|E_1|$ in the GaSb is about (4eV). The corresponding mobility is

$$\mu_{dp} = \frac{2\sqrt{2}\pi^{1/2}\hbar^4 \rho s^2 e}{3E_1^2 m^{*5/2} (kT)^{3/2}} \quad (4.14)$$

4.6.4 Acoustic phonons: piezoelectric potential

The atomic displacements produced by the acoustic-mode lattice vibrations introduce a second potential if the atoms are partially ionized. This effect, called the piezoelectric effect, occurs in the crystals lacking a center of symmetry, which includes all compound semiconductors of course. A relaxation time can be defined for the piezoelectric-potential mechanism because energy changes during the collisions are small. The relaxation time is

$$\tau_{pe} = \frac{2\sqrt{2}\pi\hbar^2 \varepsilon}{e^2 P^2 m^{*1/2} (kT)} E^{1/2} \quad (4.15)$$

where h_{pz} is the piezoelectric constant, and $P \equiv (h_{pz}^2 / \rho s^2 \varepsilon)^{1/2}$ is the piezoelectric coupling coefficient. In GaSb, P is usually given as (0.298). The mobility for the piezoelectric scattering is

$$\mu_{pe} = \frac{16\sqrt{2}\pi^{1/2}\varepsilon\hbar^2}{3eP^2m^{*3/2}(kT)^{1/2}} \frac{cm^2}{V-s} \quad (4.16)$$

4.6.5 Optical phonons: polar

The scattering mechanism due to dipole moments formed by the interaction of the ionic charges on the atoms with the optical-mode lattice vibration is polar phonon scattering. The mobility for the polar phonon scattering is

$$\mu_{po} = \frac{2^{9/3}\pi^{1/2}\hbar^2(kT)(e^{T_{po}/T}-1)\chi(T_{po}/T)}{3e(kT_{po})m^{*3/2}(\varepsilon_{\infty}^{-1}-\varepsilon^{-1})} \frac{cm^2}{V-s} \quad (4.17)$$

where $\chi(T_{po}/T)$ is a slowly varying function of T and T_{po} for GaSb is 345K.

For $0 \leq T_{po}/T \leq 5$ ($84K \leq T \leq \infty$),

$$\chi(T_{po}/T) = 1 - 0.5841(T_{po}/T) + 0.292(T_{po}/T)^2 - 0.037164(T_{po}/T)^3 + 0.0012016(T_{po}/T)^4$$

For $5 \leq T_{po}/T \leq \infty$ ($0 \leq T \leq 84K$)

$$\chi(T_{po}/T) = \frac{3\pi^{1/2}}{8} \left[\frac{T_{po}}{T} \right]^{1/2}$$

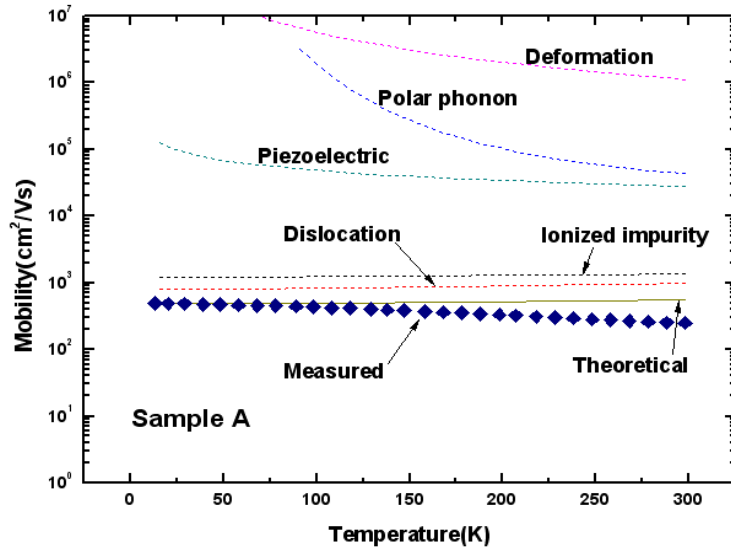
4.6.6 Matthiessen's rule

When several scattering mechanisms are simultaneously present, then the total mobility is given

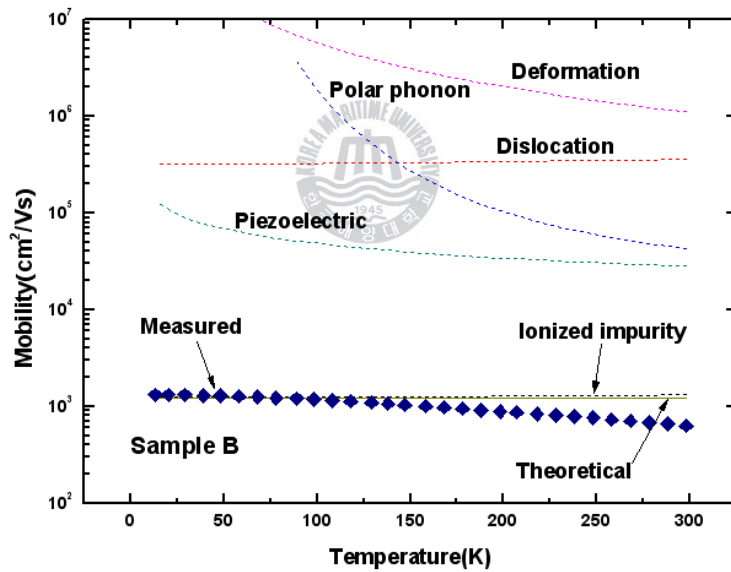
$$\mu_{total}^{-1} = \frac{1}{\sum_i \mu_i} \quad (5.18)$$

Among five scattering mechanisms, ionized impurity and dislocation are dependent on sample, i.e, $N_I = (n + N_A)$ and N_{dis} are sample dependent. Since the values of n , N_A , and N_{dis} were determined by fitting the temperature dependent concentration curves, we could calculate theoretical mobility curves for the GaSb:Te epitaxial layers. Fig. 4.7 shows the calculated (theoretical) mobilities based on five scattering mechanisms and measured mobility curves from the GaSb:Te epitaxial layers.





(a)



(b)

Fig. 4.7 Calculated (theoretical) and measured mobilities as a function of temperature for (a) sample A- GaSb:Te/GaAs (Type I) and (b) sample B- GaSb:Te/ZnTe/GaAs (Type II)

Chapter 5 Conclusion

In this study the role of ZnTe buffer on the electrical transport properties of GaSb:Te epitaxial layers grown on GaAs substrate using Molecular Beam Epitaxy (MBE) was investigated.

For the GaSb:Te/ZnTe/GaAs epitaxial layer (Type II), the theoretical curve obtained by combining all scattering mechanisms is nearly the same to the single mobility curve of the ionized impurity scattering because it has low dislocation density than Type I.

However, dislocation scattering is more dominant and affects the theoretical curve than ionized impurity scattering for GaSb:Te/ GaAs (Type I). When a dislocation charged, a space charge is formed around it and scatters electrons traveling across the dislocation, and thus the charged dislocation reduces the mobility. Therefore, Type II has higher mobility than Type I because of the lower dislocation density.

It can be concluded that ZnTe buffer layer has played a prominent role and improved to minimize the threading dislocation density which is originating from the GaSb/GaAs interface to the GaSb thin films during epitaxial growth of GaSb:Te epitaxial layers but also gives higher electrical properties than without using buffer layer. Consequently, this study should be more vigorously pursued to the implementation of optoelectronic devices.

References

- [1] R. A. Laudise, *J. Cryst. Growth* 65, 3 (1983).
- [2] Special Issue on Low Fibres, *IEEE Lightwave Technol.* LT-2 (1984).
- [3] A.G. Milnes and A. Y. Polyakove, *Solide-State Electron.* 36,803 (1993).
- [4] H. Xie, J. Piao, J. Katz, and W.I, *J.Appl.Phys.*70,3152 (1991).
- [5] V. Swaminathan and A. T. Macrander, *Material aspects of GaAs and InP based structures* (Prentice-Hall,Englewood Cliffs, NJ, 1991), Chap. 1.
- [6] G.Motosugi and T.Kwagawa, *Jpn. J. Appl, Phys.* 19,2303 (1980)
- [7] M. B. Z. Morosimi, J. L. Herrera-Perez, M. S. S. Loural, A. A. G. Von Zuben, A. C. F. da Silveria, and N. B. Patel, *IEEE J. Quantum Electron.* QE-29, 2103 (1993).
- [8] Hildebrand, W. Kuebart, K.W. Benz, and M. H. Pilkuhn, *IEEE J. Quantum Electron*, QE-17, 284 (1981); see also O. Hildebrand, W. Kuebart, and M. H. Pilkuhn, *Appl. Phys. Lett.* 37,801 (1980).
- [9] K. Segawa, H. Miki, M. Otsubo, and K. Shirata, *Electron. Lett.* 12, 124 (1976).
- [10] C. Hilsum and H. D. Rees, *Electron. Lett.* 6,277 (1970).
- [11] L. Esaki, *J. Cryst. Growth* 52, 227 (1981).
- [12] L. M. Frass, G. R. Girard, J. E. Avery, B. A. Arau, V.S. Sundaram, A.G. Thompson, and J. M. Gee, *J. Appl. Phys*, 66, 3866 (1989).
- [13] See the NESTCAPE homepages: DRA highlights, diode laser gas sensors, etc.
- [14] P. S. Dutta, Ph.D. thesis, Indian Institute of Science, Bangalore, India, 1995.
- [15] G. Benz and R. Conradt, *Phys, Rev. B* 16, 843 (1977).
- [16] G. Muller, *J. Cryst. Growth* 99, 1242 (1990).
- [17] R. D. Baxater, R.T. Bate, and F. J. Reid, *J. Phys, Chem, Solids* 26, 41 (1965).
- [18] F.J. Reid, R. D, Baxter and S. E. Miller, *J. Electronchem. Soc.* 133. 713 (1996).

- [19] C. Anayama, T. Tanahashi, H. Kuwatsuka, S. Nishiyama, S. Isozumi, and K. Nakajima, *Appl. Phys. Lett.* 56, 239 (1990).
- [20] K. F. Longenbach and W. I. Wang, *Appl. Phys. Lett.* 59, 2427 (1991).
- [21] W. Lee, S. Kim, S. Choi, H. C. Lee and J. Chang, *J. Cryst. Growth* 305, 44 (2007)
- [22] M. E. Straumanis and C. D. Kim, *J. Appl. Phys.* 36, 3822 (1965)
- [23] V. M. Glazov, S. N. Chizhevskaya, and S. B. Evgen'ev, *Zh. Fiz. Khim.* 43, 373 (1969).
- [24] F. Donald Bloss, *Crystallography and Crystal Chemistry: An Introduction* (Holt, Rinehart and Winston, New York, 1971).
- [25] K. Aoki, E. Anastassakis, and M. Cardona, *Phys. Rev. B* 30, 681 (1984).
- [26] U. Piesbergen, in *Semiconductors and Semimetals*, edited by R. K. Willardson and A. C. Beer (Academic, New York, 1966), Chap. 3, Vol. 2.
- [27] N. M. Kochetkora and T. N. Rezukhina, *Chem. Abstracts* 56, 4167E (1962).
- [28] M. G. Holland in *Semiconductors and Semimetals*, edited by R. K. Willardson and A. C. Beer (Academic, New York, 1966), Chap. 1, Vol. 2. (1962).
- [29] S. J. Fray, F. A. Johnson, and R. H. Jones, *Proc. Phys. Soc. London* 76, 939 (1960).
- [30] W. Cochran, S. J. Fray, J. E. Quarrington, and N. Williams, *J. Appl. Phys.* 32, 2102 (1961).
- [31] S. K. Joshi and S. S. Mitra, *Proc. Phys. Soc. London* 76, 295 (1960).
- [32] J. K. D. Verma, B. D. Nag, and P. S. Nair, *Z. Naturforschung* 19a, 1561 (1964).
- [33] E. F. Steigmeier, *Appl. Phys. Lett.* 3, 6 (1963).
- [34] W. F. Boyle and R. J. Sladek, *Phys. Rev. B* 11, 2933 (1975).
- [35] M. K. Farr, J. G. Taylor, and S. K. Sinha, *Phys. Rev. B* 11, 1587 (1975).
- [36] P. B. Klein and R. K. Chang, *Phys. Rev. B* 14, 2498 (1976).

- [37] S. I. Novikova and N. Kh. Abrikosov, *Sov. Phys. Solid State* 5, 1558 (1963).
- [38] L. Bernstein and R. J. Beals, *J. Appl. Phys.* 32, 122 (1961).
- [39] S. I. Novikova, in *Semiconductors and Semimetals*, edited by R. K. Willardson and A. C. Beer (Academic, New York, 1966), Vol. 2, Chap. 2.
- [40] M. G. Holland, *Phys. Rev.* 134, A471 (1964).
- [41] M. G. Holland, *Proc. Int. Conf. Phys. Semicond. Paris*, (1964), p. 713.
- [42] J. M. Ziman, *Philos. Mag.* 1, 191 (1956).
- [43] R. W. Keyes, *Phys. Rev.* 122, 1171 (1961).
- [44] Griffin and P. Carruthers, *Phys. Rev.* 131, 1976 (1963).
- [45] E. F. Steigmeier and I. Kudman, *Phys. Rev.* 141, 767 (1966).
- [46] E. F. Steigmeier and I. Kudman, *Phys. Rev.* 132, 508 (1963).
- [47] J. R. Chelikowsky and M. L. Cohen, *Phys. Rev. B* 14, 556 (1976).
- [48] T. C. Chiang and D. E. Eastman, *Phys. Rev. B* 22, 2940 (1980).
- [49] D. E. Aspnes, C. G. Olson, and D. W. Lynch, *Phys. Rev. B* 14, 4450 (1976).
- [50] W. Ruhle, W. Jakowetz, C. Woelk, R. Linnebach, and M. Pilkuhn, *Phys. Status Solidi B* 73, 225 (1973).
- [51] Joullie, A. Z. Eddine, and B. Girault, *Phys. Rev. B* 23, 928 (1981).
- [52] Madelung, *Physics of III-V Compounds* (Wiley, New York, 1964).
- [53] C. Alibert, A. Joullie, A. M. Joullie, and C. Ance, *Phys. Rev. B* 27, 4946 (1983).
- [54] C. D. Kourkoutas, P. D. Bekris, G. J. Papaioannou, and P. C. Euthymiou, *Solid State Commun.* 49, 1071 (1984).
- [55] Kopylov, *Solid State Commun.* 56, 1 (1985).
- [56] M. Reine, R. L. Aggarwal, and B. Lax, *Phys. Rev. B* 5, 3033 (1972).
- [57] G. Dresselhaus, A. F. Kip, and C. Kittel, *Phys. Rev.* 98, 368 (1955).
- [58] P. C. Mathur and S. Jain, *Phys. Rev. B* 19, 3152 (1979).
- [59] M. W. Heller and R. G. Hamerly, *J. Appl. Phys.* 57, 4626 (1985).

- [60] J. L. Robert, B. Pistoulet, D. Barjon, and A. Raymond, *J. Phys. Chem. Solids* 34, 2221 (1973).
- [61] J. D. Wiley, in *Semiconductors and Semimetals*, edited by R. K. Willardson and A. C. Beer (Academic, New York, 1975), Vol. 10.
- [62] R. A. Stradling, *Phys. Lett.* 20, 217 (1966).
- [63] D. A. Hill and C. F. Schwerdtfeger, *J. Phys. Chem. Solids* 35, 1533 (1974).
- [64] H. J. Lee and J. C. Woolley, *Can. J. Phys.* 59, 1844 (1981).
- [65] M. E. Lee, I. Poole, W. S. Truscott, I. R. Cleverley, K. E. Singer, and D. M. Rohlfiing, *J. Appl. Phys.* 68, 131 (1990).
- [66] Sagar, *Phys. Rev.* 117, 93 (1960).
- [67] J. Strauss, *Phys. Rev.* 121, 1087 (1961).
- [68] T. O. Yep and W. M. Becker, *J. Appl. Phys.* 37, 456 (1966).
- [69] R. D. Baxter and F. J. Reid, *Bull. Am. Phys. Soc.* 10, 599 (1965).
- [70] D. Long and R. J. Hager, *J. Appl. Phys.* 36, 3436 (1965).
- [71] D. Long, J. D. Zook, P. W. Chapman, and O. N. Tufte, *Solid State Commun.* 2, 191 (1964).
- [72] R. D. Baxter, F. J. Reid, and A. C. Beer, *Phys. Rev.* 162, 718 (1967).
- [73] H. Brooks, in *Advances in Electronics and Electron Physics* (Academic, New York, 1955), Vol. 7, p. 156.
- [74] Lebedev and I. A. Strel'nikova, *Sov. Phys. Semicond.* 13, 229 (1979).
- [75] E. J. Johnson, I. Filinski, and H. Y. Fan, in *Report of the International Conference on the Physics of Semiconductors, Exeter, 1962* (The Institute of Physics and The Physical Society, London, 1962), p. 375.
- [76] K. Nakashima, *Jpn. J. Appl. Phys.* 20, 1085 (1981).
- [77] M. A. Habegger and H. Y. Fan, *Phys. Rev.* 138, 598 (1965).
- [78] K. Lazareva and V. M. Stuchechnikov, *Sov. Phys. Semicond.* 4, 550 (1970).
- [79] S. Kyuregyan, I. K. Lazareva, V. M. Stuchechnikov, and A. E. Yunovich, *Sov. Phys. Semicond.* 6, 208 (1972).

- [80] M. D'Olne Campos, A. Gousskov, L. Gousskov, and J. C. Pons, *Phys. Status Solidi A* 2, 779 (1970).
- [81] T. O. Yep and W. M. Becker, *Phys. Rev.* 144, 741 (1966).
- [82] D. Kranzer, *Phys. Status Solidi A* 26, 11 (1974).
- [83] J. Kolodziejczak, S. Zukotynski, and H. Stramska, *Phys. Status Solidi* 14, 471 (1966).
- [84] P. S. Dutta, V. Prasad, H. L. Bhat, and Vikram Kumar, *J. Appl. Phys.* 80, 2847 (1996); see also P. S. Dutta, B. Mendez, J. Piqueras, E. Dieguez, and H. L. Bhat, *ibid.* 80, 1112 (1996).
- [85] G. R. Johnson, B. C. Cavenett, T. M. Kerr, P. B. Kirby, and C. E. C. Wood, *Semicond. Sci. Technol.* 3, 1157 (1988).
- [86] H. N. Leifer and W. C. Dunlap, Jr., *Phys. Rev.* 95, 51 (1954).
- [87] M. Kodama and M. Kimata, *J. Cryst. Growth.* 73, 641 (1985).
- [88] K. F. Longenbach and W. I. Wang, *Appl. Phys. Lett.* 59, 2427 (1991).
- [89] S. M. Newstead, T. M. Kerr, and C. E. C. Wood, *J. Appl. Phys.* 66, 4184, (1989).
- [90] S. Subanna, G. Tuttle and H. Kromer, *J. Electron. Mater.* 17, 297, (1989).
- [91] Y. Zhu, Y. Takeda, and A. Sasaki, *J. Appl. Phys.* 64, 1897 (1988).
- [92] I. Poole, M. E. Lee, A. R. Peaker and K. E. singer, *Appl. Phys. Lett.* 57, 1645 (1990).
- [93] S.J. Eglash, H. K. Choi and C. W. Turner, *J. Cryst. Growth* 111, 601 (1991).
- [94] T. H. Chin, W. T. Sang and N. T. Ha, *appl. Phys. Let.* 56, 1688 (1990).
- [95] N. A. Goryunova, *The Chemistry of Diamond-Like Semiconductors*, (MIT Press, Lancaster, England, 1965) p.122.
- [96] D. R. Lide, Ed., *Handbook of Chemistry and Physics*, (75th ed., CRC Press, Boca Raton, FL, 1994) p.1444.
- [97] D. T. F. Marple, *J. Appl.Phys.*, 35, 1879, (1964).

- [98] M. Shur, *Physics of Semiconductor Devices*, (Prentice-Hall, Englewood Cliffs, NJ, 1990) p.633.
- [99] S. I. Novikova and N. Kh. Abrikosov, *Sov. Phys. Solid State*, 5, 158, (1969).
- [100] J. Carides and A. G. Fisher, *Solid State Commun.*, 2, 217, (1964).
- [101] F. Kelemen, E. Cruceanu, and D. Niculescu, *Phys. Status Solidi*, 11, 865, (1965).
- [102] N. A. Goryunova, (Solzhnyye Almazopodobnyye Poluprovodniki (Multinary Diamond-Like Semiconductors), Soviet Radio, Moscow, 1968) p.106.
- [103] D. A. Berlincourt, H. Jaffe, and L. R. Shiozawa, *Phys. Rev.*, 129, 1009, (1963).
- [104] H. Tubota, *Jpn. J. Appl. Phys.*, 2, 259, (1963).
- [105] S. Larach, R. E. Sharder, and C. F. Stocker, *Phys. Rev.*, 108, 587, (1957).
- [106] M. Cardona and D. L. Greenaway, *Phys. Rev.*, 131, 98, (1963).
- [107] C. Aten, c. Z. Van Doorn, and A. T. Vink, *Proc. Int. Conf. Phys. Semicond.*, Exeter, 1962. *Phys. Soc. London*, 696, (1962).
- [108] Data in Science and Technology, R. Poerschke, Ed., *Semiconductors Others Than Group IV Elements and III-V Compounds*, O. Maselung, Ed., Springer-Verlag, New York, (1992) p.28.
- [109] M. Cardona, *J. Phys. Chem Solids*, 24, 1543, (1963); 26, 1351, (1965).
- [110] M. Shur, *Physics of Semiconductor Devices*, (Prentice-Hall, Englewood Cliffs, NJ, 1990) p.633.
- [111] M. Aven and B. Segall, *Phys. Rev.*, 130, 81, (1963).
- [112] V. M. Glazov, S. N. Chizhevskaya, and N. N. Glagoleva, *Zhidkiye Poluprovodniki (Liquid Semiconductors)*, Nauka, Moscow, (1967).
- [113] E. Raiskin, Rais Enterprises, Inc. Catalog, (1994).
- [114] G. Fischer, J. N. Cardies and J. Drescher, *Solid State Commun.*, 2, 157, (1964).
- [115] M. Aven and J. S. Prener, Eds., *Physics and Chemistry of II-VI Compounds*, John Wiley & Sons, (1967).

- [116] David C. Look, *Electrical Characterization of GaAs materials and devices*, (John Wiley & Sons. 1989) p2.
- [117] David C. Look, *Electrical Characterization of GaAs materials and devices*, (John Wiley & Sons. 1989) p10.
- [118] D. K. Bowen and B. K. Tanner, *High Resoultion X-Ray Diffractometry and Topography*, (Taylor & Francis ltd, London, United Kingdom, 1998), p4.
- [119] G. Bauer, W. Richter, *Optical Characterization of Epitaxial Semiconductor Layers*, Springer, p297.
- [120] D. K. Bowen and B. K. Tanner, *High Resoultion X-Ray Diffractometry and Topography*, (Taylor & Francis ltd, London, United Kingdom, 1998), p52.
- [121] D. C. Look and R. J. Molnar, *Appl. Phys. Lett.* 70, 3377, (1997).
- [122] D. C. Rook and J. R. Sizelove, *Phy. Rev. Lett.* 82, 1237, (1999).
- [123] David C. Look, *Electrical Characterization of GaAs materials and devices*, (John Wiley & Sons. 1989) Ch.2.
- [124] D. C. Look, C. E. Stuz, R. J. Molnar, K. Saarinen, and Z. Lilental-Weber, *Solid State Commun.* 117, 571, (2001).
- [125] D. L. Rode, *Semicond. Semimet.* 10, 1 (1975).